RESEARCH ARTICLE | DECEMBER 12 2022

Effect of interaction strength on recovery downstream of incident shock interactions

Fulin Tong (童福林); Jiang Lai (赖江); Junyi Duan (段俊亦); ... et. al

Physics of Fluids 34, 125127 (2022)
https://doi.org/10.1063/5.0130596

Physics of Fluids ARTICLE scitation.org/journal/phf

Effect of interaction strength on recovery downstream of incident shock interactions

Cite as: Phys. Fluids **34**, 125127 (2022); doi: 10.1063/5.0130596
Submitted: 13 October 2022 · Accepted: 23 November 2022 ·
Published Online: 12 December 2022

Fulin Tong (童福林),[1] Jiang Lai (赖江),[1] Junyi Duan (段俊亦),[2,3] Siwei Dong (董思卫),[1] Xianxu Yuan (袁先旭),[1,a)] and Xinliang Li (李新亮)[2,3]

AFFILIATIONS

[1]State Key Laboratory of Aerodynamics, 621000 Mianyang, China
[2]LHD, Institute of Mechanics, Chinese Academy of Sciences, 100190 Beijing, China
[3]School of Engineering Science, University of Chinese Academy of Sciences, 100049 Beijing, China

[a)]Author to whom correspondence should be addressed: yuanxianxu@cardc.cn

ABSTRACT

Direct numerical simulations of a supersonic turbulent boundary layer on a flat plate interacting with an impinging shock wave are carried out with two different incident shock angles at Mach 2.25. The effect of the interaction strength on the recovery process in the downstream region is systematically studied, including the turbulence evolution, the statistical and structural properties of wall pressure fluctuations, and the generation of mean skin friction and wall heat flux. The variations of the Reynolds stress components, the anisotropy tensor, and the turbulent kinetic energy budget in the two flow cases highlight a slow reversal tendency and an increasingly pronounced importance of the outer-layer large-scale structures in the relaxation region of the strong interaction. We find that the effect of increasing the interaction strength on the fluctuating wall pressure is reflected by a decrease in the characteristic frequencies, an increase in the spatial extent, and a decrease in the convection velocity. We decompose the mean skin friction and wall heat flux into different physically informed contributions and reveal that the mean wall heat flux generation is the same regardless of the interaction strength; in contrast, the generation mechanism of mean skin friction is found to be fundamentally changed. A novel scale-decomposition method is used to quantify the effect of the increased interaction strength on the leading components, and it is demonstrated that the energetic outer-layer large-scale structures are the dominant contributor in the recovery process as the interaction strength is increased.

I. INTRODUCTION

Because of its importance in a wide range of high-speed external and internal flow applications, the flow phenomena associated with shock-wave/turbulent-boundary-layer interactions (SWTBLIs) have been extensively studied for more than 60 years. Notable reviews of prior work on this topic have been given by Dolling[1] and Gaitonde.[2] It is well known that the interaction strength is an important factor governing these interactions; an increased interaction strength can change the flow topology and bring about large separation, high pressure, and high thermal loads in the interaction region. Improving the basic understanding of flow behavior associated with different interaction strengths is helpful for the novel design of flow-control methodologies and thermal-protection systems.

Significant progress has been made regarding the effect of the interaction strength on the unsteadiness in a number of SWTBLI flows. The majority of previous studies have focused on two canonical flow configurations: compression ramp interactions and incident shock interactions. This is particularly the case for broadband shock oscillations, even though the driving mechanism responsible for the low-frequency large-scale unsteadiness of shock motion is still under debate, as reviewed by Clemens and Narayanaswamy.[3] Generally, variation of the interaction strength is achieved by adjusting the ramp angle or the angle of the incident shock; i.e., a larger angle is used to induce a stronger interaction. For example, in experiments with several two-dimensional compression ramps at Mach 3 and Reynolds number $Re_\infty = 1.4 \times 10^6$ (based on the incoming boundary layer thickness), Dolling and Or[4] measured wall pressure fluctuations in four ramps with angles of 20°, 16°, 12°, and 8°. They found an unsteady intermittent region in both the attached and separated cases and suggested that there was significant low-frequency energy in the separated flows. Dupont *et al.*[5] experimentally studied the time and length scales of the unsteady shock motion in a Mach 2.3 impinging shock interaction for a wide range of shock intensities. They found a strong statistical link between the low-frequency unsteadiness and the downstream

interaction and proposed dimensionless frequencies to characterize low-frequency shock unsteadiness. Morgan *et al.*[6] performed a parametric study based on large-eddy simulations (LES) of the interaction of an oblique shock impinging on a Mach 2.28 turbulent boundary layer (TBL) for seven different wedge angles to analyze the effect of the interaction strength on the low-frequency unsteadiness. It was highlighted that an increased shock-generating wedge angle resulted in a significant increase in the intensity of low-frequency oscillations, with the timescales becoming longer. Using the LES database, they assessed the commonly cited upstream and downstream mechanisms in previous studies and suggested that the low-frequency unsteadiness in the case of the strongest interactions was probably not driven by the upstream dynamics.

Souverein *et al.*[7] used two-component planar particle image velocimetry to examine shock reflections with varying incident shock angles; they investigated how the shock unsteadiness mechanism varied as a function of the imposed shock intensity. Conditional statistics based on the separation bubble height revealed that the large-scale low-frequency shock motions were strongly correlated with the pulsation of the separation bubble, confirming the predominance of downstream unsteadiness in the early experimental findings of Dupont *et al.*[5] Furthermore, they proposed that the upstream and downstream mechanisms coexist, and which mechanism dominates will depend on the interaction strength. It was argued that the dynamics of the separation bubble govern the flow unsteadiness in strong interactions, while the upstream fluctuations become dominant in weak interactions with no separation; they noted that a superposition of upstream and downstream mechanisms, with a weighting function depending on the flow state, can be expected for the timescales in the incipient cases.

In recent years, the effect of the interaction strength on turbulent structures and their statistics in the interaction zone for canonical SWTBLIs has also attracted a relatively limited number of numerical and experimental investigations. The results of the LES by Morgan *et al.*[6] of impinging SWTBLIs suggested that the turbulent kinetic energy (TKE) budget terms obeyed a trend of increasing magnitude upstream and decreasing magnitude downstream with increasing wedge angle. Later, Jammalamadaka *et al.*[8] performed direct numerical simulations (DNS) of shock reflections at three different incident angles to uncover the effect of the interaction strength on the terms contributing to the TKE and enstrophy budgets. They found a strong and dynamic coupling between the turbulence and the mean flow in the interaction region, which was remarkable for higher shock intensities. Schreyer *et al.*[9] employed particle image velocimetry to examine an attached 8° compression corner and a fully separated 33° ramp at Mach 7.2. Surprisingly, they found that the turbulent structure characterized by the anisotropy parameter developed more rapidly in the stronger interaction. They explained that this behavior results from the interaction in the attached cases enhancing the wall-normal mixing, whereas the streamwise and wall-normal mixings are approximately equally enhanced in the separated cases. The results of experiments examining a Mach 2.8 flow over 8°, 16°, 24°, and 32° compression ramps conducted by Mustafa *et al.*[10] suggested that the wall-normal integrated streamwise TKE scales as an exponential with respect to the ramp angle. Furthermore, they applied snapshot proper orthogonal decomposition (POD), and the resulting POD spectrum featured an inertial range common to the boundary layer. Most of the kinetic energy was contained in these first POD modes (except the 8° case with the mostly attached flow), which dominated the separation bubble filling/collapse and oscillation.

In the present study, we aim to investigate the effect of the interaction strength on the development of the boundary layer downstream of an incident shock interaction using DNS. This shock interaction often results in peak pressure and heat loads in the downstream region; this phenomenon is not yet fully understood, and it cannot be satisfactorily predicted by existing turbulence models with additional corrections, as concluded by Babinsky and Harvey.[11] It is generally accepted that the surface quantities in weak interactions can be predicted with confidence, but significant differences between experimental results and Reynolds-averaged Navier–Stokes simulations are obtained for strong interactions with separations, and the deviations can be as great as 100%. This work is motivated by this gap in understanding. In light of this gap, we perform two DNS studies of an oblique shock impinging on a Mach 2.25 turbulent boundary layer. The same inflow conditions are used, but two shock angles, $\beta = 29°$ and 33.2°, are selected, corresponding to weak and strong interactions, respectively; accordingly, the mean flows in these interactions are, respectively, attached and separated. The present work focuses, in particular, on a comparative analysis of turbulence evolution, wall pressure fluctuations, and decomposition of mean skin friction and wall heat flux (WHF). The main objectives of the present study are to discuss not only the effect of the interaction strength on the characterizations of turbulent structures and fluctuating wall pressure but also the quantitative contributions of various turbulent scales to the mean skin friction and WHF generation.

To this end, in this paper, spectral decomposition of turbulent fluctuations based on the pre-multiplied spanwise energy spectra is used to characterize the roles of small- and large-scale structures in the boundary layer relaxation process. The global fluctuating wall pressure fields in the downstream region are examined mainly by space–time correlation analysis; it is difficult to obtain these measurements reliably and accurately in experiments. Finally, the theoretical decompositions proposed by Li *et al.*[12] and Sun *et al.*[13] are used to highlight the quantitative contributions of various turbulent scales to the generation of mean skin friction and WHF. A similar decomposition approach can be found in our previous works examining a zero-pressure-gradient supersonic turbulent boundary layer[14] and an impinging SWTBLI[15] at Mach 2.25, where bidimensional empirical mode decomposition was chosen to split the fluctuations into four modes with increasing characteristic spanwise length scales. In this paper, we analyze the scale-decomposed contributions based on cospectra of the Reynolds shear stress and wall-normal heat flux, anticipating that this comparison will reveal direct scale-dependent differences between the weak and strong interactions.

The remainder of this paper is organized as follows: in Sec. II, details of the two DNS studies performed in the present work are introduced, including their governing equations, the computational setup, and validation of the DNS data. The effect of the interaction strength on boundary layer recovery downstream of the interaction is given and discussed in Sec. III. Finally, concluding remarks are presented in Sec. IV.

II. DIRECT NUMERICAL SIMULATIONS

A. Governing equations and numerical methods

The governing equations are the full three-dimensional compressible conservative Navier–Stokes equations for a perfect gas in Cartesian coordinates (x, y, z), which are non-dimensionalized by inflow parameters,

$$\frac{\partial U}{\partial t}+\frac{\partial F}{\partial x}+\frac{\partial G}{\partial y}+\frac{\partial H}{\partial z}=0, \tag{1}$$

where U is the state vector; and F, G, and H denote the flux terms in the x, y, and z directions, respectively. Here, U and F are given as

$$U=\begin{bmatrix}\rho\\ \rho u\\ \rho v\\ \rho w\\ \rho E\end{bmatrix},\qquad F=F_c+F_v=\begin{bmatrix}\rho u\\ \rho u^2+p\\ \rho uv\\ \rho uw\\ (\rho E+p)u\end{bmatrix}-\begin{bmatrix}0\\ \sigma_{xx}\\ \sigma_{xy}\\ \sigma_{xz}\\ u\sigma_{xx}+v\sigma_{xy}+w\sigma_{xz}+q_x\end{bmatrix}. \tag{2}$$

Here, ρ, p, and E are the density, pressure, and total energy, respectively; u, v, and w denote the velocity components in the x, y, and z directions, respectively; and F_c and F_v represent the inviscid and viscous fluxes, respectively. The heat flux and viscous stress terms in F_v are given as

$$\begin{aligned}q_x&=-\frac{\mu}{(\gamma-1)Re_\infty PrM_\infty^2}\frac{\partial T}{\partial x},\\ \sigma_{xx}&=\frac{2\mu}{Re_\infty}\left(\frac{2}{3}\frac{\partial u}{\partial x}-\frac{1}{3}\frac{\partial v}{\partial y}-\frac{1}{3}\frac{\partial w}{\partial z}\right),\\ \sigma_{xy}&=\frac{\mu}{Re_\infty}\left(\frac{\partial u}{\partial y}+\frac{\partial v}{\partial x}\right),\\ \sigma_{xz}&=\frac{\mu}{Re_\infty}\left(\frac{\partial u}{\partial z}+\frac{\partial w}{\partial x}\right).\end{aligned} \tag{3}$$

Here, T is the temperature, Re_∞ and M_∞ represent the free-stream Reynolds number and Mach number, Pr denotes the Prandtl number, and $\gamma=1.4$ is the ratio of specific heats. The ideal-gas state equation and Sutherland's law, given as

$$\begin{aligned}p&=\frac{\rho T}{\gamma M_\infty^2},\\ \mu&=T^{3/2}\frac{1+T_s/T_\infty}{T+T_s/T_\infty},\end{aligned} \tag{4}$$

are used to link the thermodynamic variables and to calculate the dynamic viscosity coefficient μ, where $T_s=110.4\,\mathrm{K}$ and T_∞ is the free-stream temperature. In the analysis that follows, the subscript "∞" refers to the quantity in the free-stream flow. The expressions of the flux terms G and H in the y and z directions are similar to that of F, and for simplicity, these are not shown.

We directly solve the above governing equations without any modeling by using an open-source high-order finite-difference flow solver, OpenCFD-SC. This solver has recently been applied to studies of various compressible flows with great success, including compression ramp interactions,[16,17] impinging SWTBLIs,[18,19] and a hypersonic transition boundary layer.[20,21] The inviscid fluxes are discretized by the fourth-order symmetric bandwidth-optimized weighted essentially non-oscillatory (WENO) scheme proposed by Martin *et al.*[22] and later improved by Wu and Martin.[23] In particular, the bandwidth-resolving efficiency is maximized by using a symmetric collection of candidate stencils and optimizing the WENO weights. Furthermore, an absolute limiter on the WENO smooth measurement and a relative limiter on the total variation are used to further reduce numerical dissipation. Under such modifications, this scheme is low dissipative to resolve the smooth flow region, and it is also robust in regions with strong discontinuities. An eighth-order central-difference scheme is used for the viscous fluxes. For the temporal integration, the third-order total-variation-diminishing Runge–Kutta method introduced by Gottlieb and Shu[24] is employed.

B. Computational setup

Figure 1 shows a sketch of the rectangular computational domain plotted in Cartesian coordinates (x, y, z). The length in the streamwise direction (x) is $L_x=99.6\,\mathrm{mm}$, and the height and width in the wall-normal (y) and spanwise (z) directions are $L_y=10.2\,\mathrm{mm}$ and $L_z=4.4\,\mathrm{mm}$, respectively. The flow direction in the figure is from left to right. A spatially developing turbulent boundary layer (TBL) over a flat plate is made to interact with an incident oblique wave. Following the previous DNS studies of Pirozzoli *et al.*[25] and Priebe *et al.*,[26] the wedge-shaped shock generator is not included in the computational domain; instead, the impinging shock is numerically generated by imposing the Rankine–Hugoniot relations at the upper boundary of the domain. The incoming TBL is characterized by a free-stream Mach number of $M_\infty=2.25$, a free-stream temperature of $T_\infty=169.44\,\mathrm{K}$, a wall temperature of $T_w=254.16\,\mathrm{K}$, and a unit free-stream Reynolds number of $Re_\infty/\mathrm{mm}=2.5\times10^4$, in accordance with recent simulations of Tong *et al.*[14,15] The boundary layer thickness δ is estimated to be 1.27 mm at the reference point, which is located upstream of the interaction and has a streamwise distance of 63.5 mm from the domain inlet. In this study, we run two DNS cases using the same computational domain and inflow turbulence, denoted as shock29 and shock33.2, in which the shock angles are set to $\beta=29^\circ$ and 33.2°, respectively. For both cases, the nominal shock-impingement point at the wall is fixed at $x_s=71.1\,\mathrm{mm}$.

As sketched in Fig. 2, the computational domain is discretized by a grid consisting of $N_x\times N_y\times N_z=3127\times420\times340$ points in the x, y, and z directions, respectively. In the streamwise direction, the interaction region $50.8<x<90.2\,\mathrm{mm}$ is well resolved, in which a total of 2627 points are uniformly distributed, while the grid resolutions in the upstream transition zone and the downstream fringe zone are much lower, leading to 400 points gradually refined in $0<x<50.8\,\mathrm{mm}$ and 100 points progressively coarsened in $x>90.2\,\mathrm{mm}$. The grid spacing in the spanwise direction is uniform, and the points in the wall-normal direction are clustered toward the wall, ensuring that 280 points are located inside the boundary layer. In the interaction region, the grid spacing used in the present simulations is $\Delta x^+=8.5$ in the streamwise direction and $\Delta z^+=7.15$ in the spanwise direction, $\Delta y^+=0.55$ at the first grid point above the wall and $\Delta y^+=5.5$ at the edge of the turbulent boundary layer; these values are comparable to those used in the well-accepted DNS studies of SWTBLIs by Priebe *et al.*[26] and Fang *et al.*[27] Unless otherwise noted, the superscript "+" indicates that the quantity is normalized by inner-scale units at x_{ref} (e.g., friction velocity u_τ or viscous length scale δ_v).

In the present DNS, the following boundary conditions are enforced. At the domain inlet, a steady inflow laminar profile, as reported by Tong *et al.*,[14,15] is imposed. The inflow turbulence is generated by the laminar-to-turbulent transition method, where the

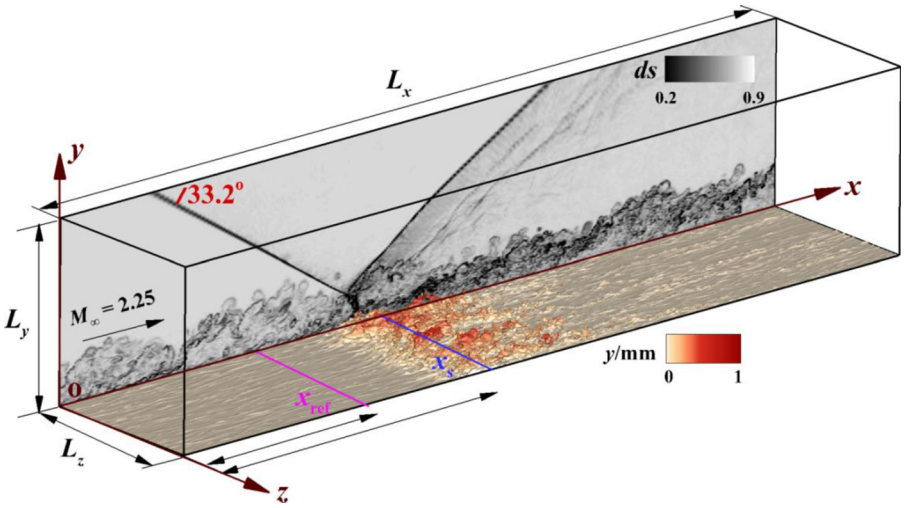

FIG. 1. Sketch of the computational domain for the impinging SWTBLIs under investigation. Contours of the instantaneous density gradient ds in the x–y plane and the iso-surface of the instantaneous streamwise velocity $u/u_\infty = 0.2$ colored by the wall-normal distance y are obtained from the DNS of shock33.2. The parameters x_{ref} and x_s denote the reference point and the nominal shock-impingement point at the wall, respectively.

unsteady wall-normal velocity disturbances introduced by Pirozzoli *et al.*[28] and Fang *et al.*[27] are only enforced in the blowing and suction region at the wall between $x_a = 7.5$ mm and $x_b = 20.2$ mm. The disturbances are expressed as $v_{bs} = Af_{bs}(x)g_{bs}(z)h_{bs}(t)$, and

$$\begin{aligned} f_{bs}(x) &= \frac{4}{\sqrt{27}}\sin\left(2\pi\frac{x-x_a}{x_b-x_a}\right)\left(1-\cos\left(2\pi\frac{x-x_a}{x_b-x_a}\right)\right), \\ g_{bs}(z) &= \sum_{l=1}^{l=10} 0.8^{l-1} g_0 \sin\left[2\pi l\left(\frac{z}{L_z}+\phi_l\right)\right], \\ h_{bs}(t) &= \sum_{m=1}^{m=5} 0.8^{m-1} h_0 \sin[2\pi m(\varpi t+\phi_m)], \\ g_0 &= 1\Big/\sum_{l=1}^{l=10} 0.8^{l-1}, \quad h_0 = 1\Big/\sum_{m=1}^{m=5} 0.8^{m-1}, \end{aligned} \tag{5}$$

where A denotes the disturbance amplitude, ϕ_l and ϕ_m denote the random numbers between 0 and 1. It was found by Tong *et al.*[14,15] that the choice of the amplitude $A = 0.15u_\infty$ and the basic frequency $\varpi = 0.157\,u_\infty/\delta_{in}$ (δ_{in} being the boundary layer thickness at the domain inlet) allows the transition process to be accelerated, and a fully developed realistic turbulent boundary layer is fast established upstream of the interaction. A combination of supersonic outflow boundary conditions imposed at the domain inlet and the progressively coarsened grid used in the fringe zone are applied to inhibit the reflection of disturbances back into the domain. A non-reflecting boundary condition is enforced at the upper boundary layer, where a jump of the flow variables obeying the Rankine–Hugoniot relations is imposed at $x = 52.8$ and 55.6 mm for shock29 and shock33.2, respectively. At the bottom wall, a constant temperature $T_w = 254.16$ K, which is prescribed to be nearly 0.75 times the recovery temperature, and a no-slip isothermal boundary condition are

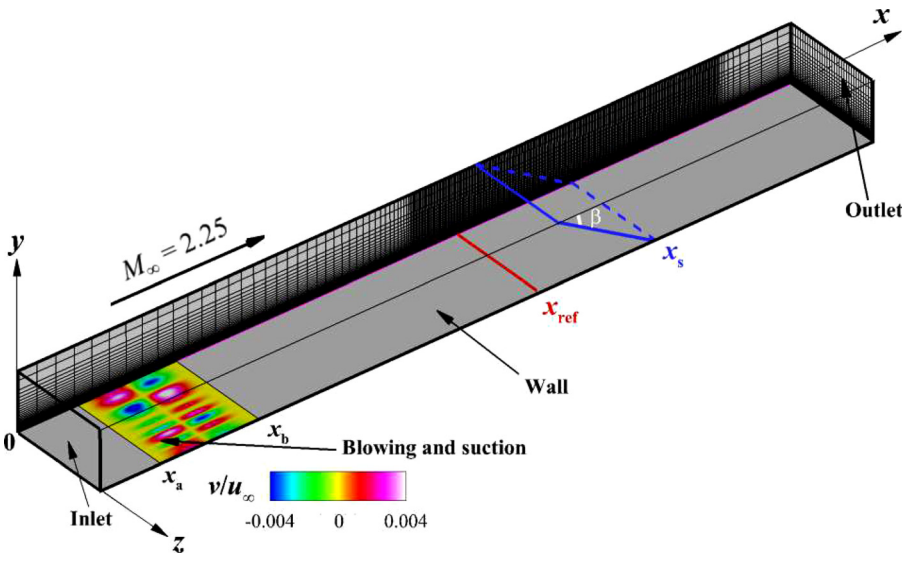

FIG. 2. Sketch of the computational grid together with the wall-normal velocity v/u_∞ in the blowing and suction region ($x_a < x < x_b$) at the wall. The grid is plotted only every tenth point, fifth point, and fifth point in the x, y, and z directions, respectively.

imposed. The domain in the spanwise direction is bounded by periodic boundary conditions.

We start the simulations by using the laminar profile at the domain inlet to initialize the three-dimensional flow field, and we perform a washout time of $127\delta/U_\infty$ (or two flow-through times). After the statistical unsteadiness is obtained, a total of 530 three-dimensional instantaneous flow fields, spanning a long time period of approximately $385\delta/U_\infty$, are collected to guarantee statistical convergence, and the full time-resolved wall pressure signals are sampled at a short time interval of $0.014\delta/U_\infty$ to accurately estimate the spatial and temporal evolution of the wall pressure fluctuations. The mean field is obtained by the average in time and in the spanwise direction. For a generic instantaneous variable φ, the decomposition $\varphi = \bar{\varphi} + \varphi'$ or the density-weighted decomposition $\varphi = \tilde{\varphi} + \varphi''$ is used, where the Reynolds and density-weighted averages are defined as $\bar{\varphi}$ and $\tilde{\varphi} = \overline{\rho\varphi}/\bar{\rho}$, respectively, with the corresponding fluctuations being φ' and φ''. Throughout this paper, δ denotes the boundary layer thickness at x_{ref}.

C. Validation

To investigate the effect of the selected spanwise width on the DNS results, we examine the distribution of the spanwise two-point correlations of velocity fluctuations in the interaction region. In Fig. 3, the correlation coefficient $R_{\alpha\alpha}$ given by Pirozzoli *et al.*[28] is reported as a function of the spanwise spacing r_z in the inner and outer regions at $(x - x_s)/\delta = 1.5$, where α denotes the fluctuations of u, v, and w, respectively. Clearly, $R_{\alpha\alpha}$ rapidly decreases as r_z gradually increases; when the spanwise spacing is close to $L_z/2$, all the correlation coefficients are maintained near zero, confirming that the spanwise width used in the present simulation is sufficient and the turbulent fluctuations are not inhibited in the spanwise direction.

Figure 4(a) compares the van Driest transformed mean streamwise velocity profile at x_{ref} with the incompressible law of the wall and the DNS data of Fang *et al.*[27] at similar friction Reynolds number and Mach number. In the figure, $\bar{u}^+_{vd}$ is calculated as

$$\bar{u}^+_{vd} = \frac{1}{u_\tau}\int_0^{\bar{u}} \sqrt{\frac{\bar{\rho}}{\bar{\rho}_w}}\mathrm{d}\bar{u}. \tag{6}$$

The agreement is satisfactory, and it can be seen that a linear scaling occurs in the inner layer for $y^+ < 6$, and a logarithmic law of the wall is expected in the log-law region for $30 < y^+ < 100$. In Fig. 4(b), it can be seen that the van Driest transformed deficit velocity compares well with the numerical results of Schlatter and Örlü[29] at $Re_\tau = 1145$ and Duan *et al.*[30] at $Re_\tau = 453.1$, suggesting that outer-layer convergence is achieved.

The accuracy of the inflow turbulence is further examined in Figs. 4(c) and 4(d), where the density-scaled root-mean-square (rms) velocity and vorticity fluctuations are reported in inner coordinates. It can be seen from Fig. 4(c) that Morkovin's scaling allows the computed DNS results to compare well with the incompressible DNS data of Wu and Moin[31] at $Re_\tau = 400$ and Spalart[32] at $Re_\tau = 280$, and supersonic DNS data of Shadloo *et al.*[33] at $Re_\tau = 500$ and Pirozzoli *et al.*[34] at $Re_\tau = 359$. In particular, the streamwise velocity fluctuations attain a maximum value of 2.9 at $y^+ \approx 14$. Consistent with the findings of del Álamo and Jiménez[35] for an incompressible channel flow at $Re_\tau = 550$ and that of Pirozzoli *et al.*[36] for a supersonic boundary layer at Mach 2 and $Re_\tau = 358$, Fig. 4(d) highlights that the spanwise component of vorticity fluctuations is dominant in the near-wall region for $y^+ < 25$, and a nearly isotropic state is found for $y^+ > 30$, where the wall-normal component attains its peak at $y^+ \approx 13$ and the streamwise component shows a local minimum at $y^+ \approx 4$. It is, thus, confirmed that the inflow turbulence generated by the laminar-to-turbulent transition method in the present study is highly reliable.

Finally, we perform a grid-sensitivity study to investigate the influence of the grid resolution on the DNS results. Here, the grid points in the interaction region for shock29 are increased by 50% in

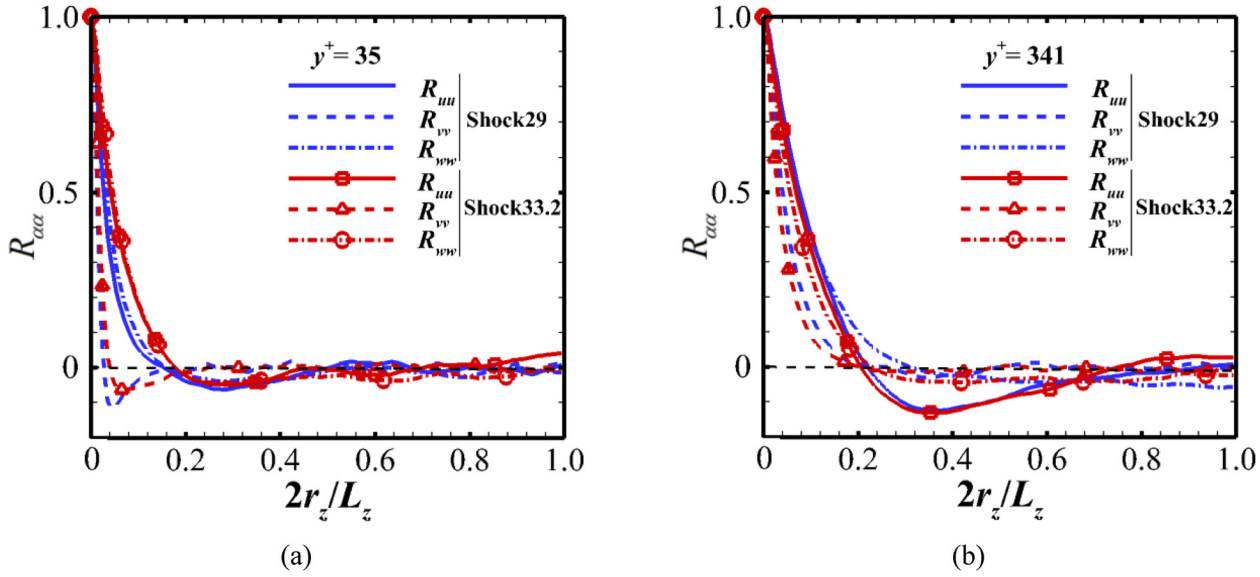

FIG. 3. Two-point correlations of velocity fluctuations as a function of spanwise distance r_z at $(x - x_s)/\delta = 1.5$: (a) $y^+ = 35$ and (b) $y^+ = 341$. R_{uu}, streamwise velocity; R_{vv}, wall-normal velocity; R_{ww}, spanwise velocity.

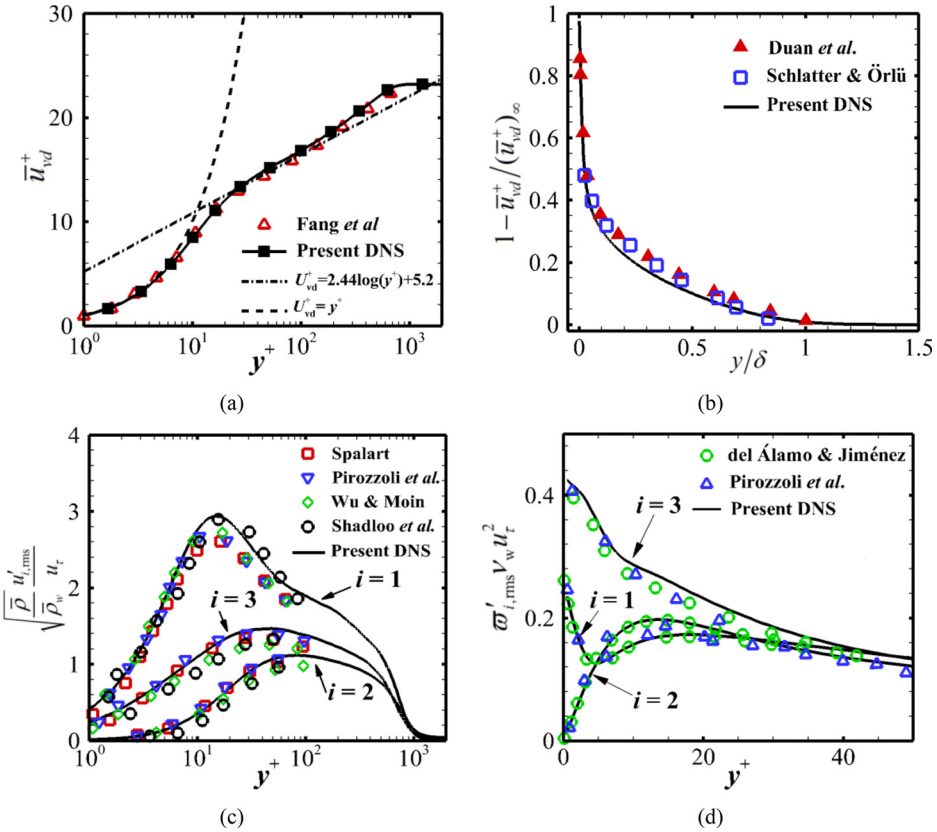

FIG. 4. Turbulence statistics at x_{ref}: (a) van Driest transformed velocity as a function of y^+; (b) van Driest transformed deficit velocity as a function of y/δ; (c) density-scaled velocity fluctuations $u'_{i,\mathrm{rms}}$; and (d) vorticity fluctuations $\varpi'_{i,\mathrm{rms}}$. Streamwise component ($i=1$), wall-normal component ($i=2$), and spanwise component ($i=3$).

both the streamwise and spanwise directions. In Fig. 5, the distributions of mean wall pressure, skin friction coefficient, and Stanton number for both grids are compared. These direct comparisons show that the mean wall pressure and Stanton number are rapidly increased across the interaction, while the skin friction experiences a sharp decrease and no negative values are found, indicating that the mean attached flow is accurately captured. It can be seen that the overall evolution is not changed by the grid refinement, and the deviations are less than $O(5\%)$, suggesting that the present grid resolution is reasonable for obtaining a grid-converged DNS simulation. Note that a similar grid refinement for shock33.2 was performed in our previous work,[15] and the mean locations of separation and reattachment were not affected.

III. RESULTS AND DISCUSSION

A. Instantaneous and mean flow fields

An overview of the flow features in the two DNS cases is first given in the x–y plane at $z=0$, where contours of instantaneous and mean temperature fields are reported in Fig. 6 and contours of instantaneous and mean streamwise velocity fields are reported in Fig. 7, respectively. As expected, a wave system consisting of the incident shock and the reflected shock becomes more evident as the interaction strength is increased. It is clear that the shock interaction significantly increases the temperature in the main stream and in the boundary layer downstream of the interaction, and this effect is remarkable for the stronger interaction. Across the interaction, the flow is decelerated for both cases. It is clearly seen from the mean streamlines in Figs. 7(b) and 7(d) that the increased interaction strength (shock33.2) induces a large region of separation bubble; conversely, no flow separation is found inside the boundary layer for shock29, confirming that the mean flow is attached.

Figure 8 shows the effect of the interaction strength on the near-wall streaks and gives a comparison of the streamwise velocity fluctuations in the x–z plane at $y^+ = 8.2$ for both cases. This figure highlights that the upstream turbulent boundary layer is characterized by canonical alternating high- and low-speed streaky structures, which are very often observed in wall-bounded turbulent flows.[37,38] It can be seen from Fig. 8(a) that the quasi-streamwise streaks are almost unchanged when the shock interaction is weak. However, in Fig. 8(b), we observe that the upstream elongated streak structures are dramatically destroyed near the shock-impingement point and are clearly regenerated in the downstream region at $(x-x_s)/\delta > 5$. This is mainly attributed to the occurrence of the separation bubble in the strong interaction, as previously discussed by Fang *et al.*[27] and Grilli *et al.*[39]

Figure 9 shows iso-surfaces of the Q criterion[40] for shock29 and shock33.2 to characterize the turbulent structures upstream and downstream of the shock interaction at a given time instant. A relatively large positive value of $Q = 22.3\,U_\infty^2/\delta^2$ is used to visualize the detected turbulent structures. The iso-surfaces are colored by the normalized wall-normal distances, and contours of the instantaneous pressure-gradient modulus in the x–y plane at $z=0$ are also included for comparison. Consistent with previous studies of zero-pressure-gradient

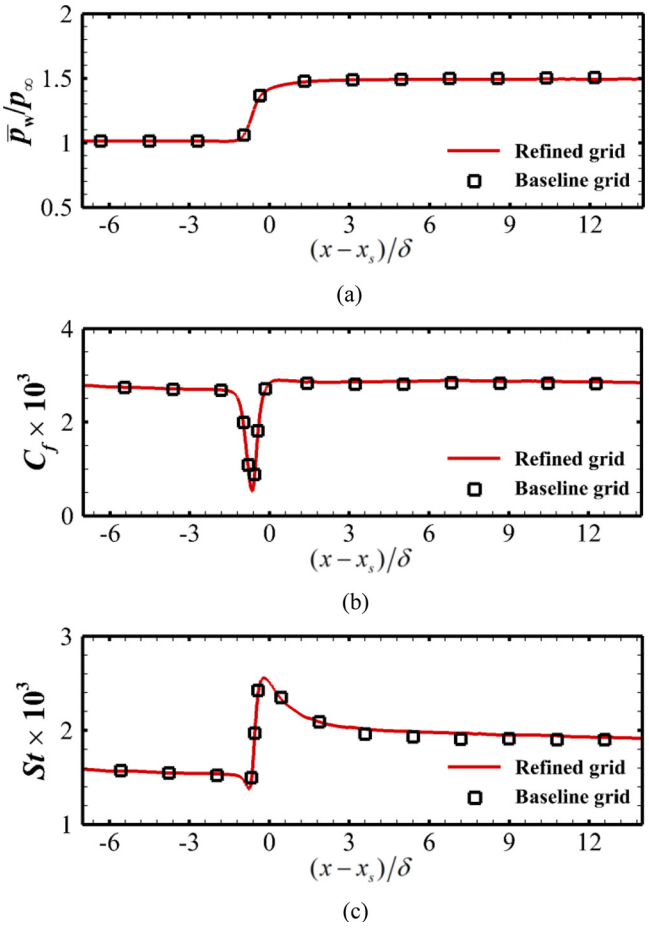

FIG. 5. Grid-sensitivity study with respect to mean properties for shock29: (a) wall pressure $\bar{p}_w/p_\infty$, (b) skin friction coefficient $C_f = 2(\mu\partial\bar{u}/\partial y)_w/\rho_\infty u_\infty^2$, and (c) Stanton number $St = (\mu\partial\bar{T}/\partial y)_w/\rho_\infty U_\infty Pr(T_w - T_r)$.

boundary layers, the incoming flow exhibits an intermittent elongated streaky character. From the turbulent structures in the downstream region, we can see an augmentation caused by the shock interaction for both cases. Compared to shock29, the turbulence for shock33.2 is significantly amplified in the outer layer, as shown at $(x - x_s)/\delta > 0$ in Fig. 9(b); here, large structures are grouped together, and they merge into larger coherent structures downstream of the interaction, leading to a much more compact behavior.

The profiles of mean wall pressure for the two cases, as shown in Fig. 10(a), exhibit a sharp rise near the shock-impingement point and a slower growth in the downstream region. It is expected that the increased interaction strength induces an upstream shift at the beginning of the pressure rise and a stronger adverse pressure gradient (APG) across the interaction. In the downstream region, Fig. 10(b) shows that the APG has an abrupt decrease, approaching zero, and near collapse of the two cases is found at $(x - x_s)/\delta > 3$. According to the mean pressure gradient parameter $\delta^*(d\bar{p}_w/dx)/\rho_w u_\tau^2$ in the figure inset, the flow in the recovery region of the shock29 case is nearly in equilibrium at $(x - x_s)/\delta > 3$, whereas no equilibrium at $(x - x_s)/\delta < 9$ is attained in the shock33.2 case. In Fig. 10(c), a sharp decrease of the skin friction coefficient is observed across the interaction for both cases due to the deceleration of the flow, whereas a different recovery behavior is clearly identified downstream of the interaction. For shock29, no negative values of C_f are found, and the value of C_f quickly increases from 0.0005 to 0.002 88, attaining a plateau at $(x - x_s)/\delta > 0$. In contrast to this, the value of C_f becomes negative in the shock33.2 case, proving the existence of a separation bubble. One interesting thing to note is that the rate of increase of C_f in the downstream region is much slower than that of shock29, despite the two cases yielding a good collapse at $(x - x_s)/\delta > 9$. This will be discussed further in Sec. III D.

A comparison of the mean wall heat flux profiles is given in Fig. 10(d). The overall distributions for the two cases are similar. It can be seen that C_h first experiences a slight decrease in the vicinity of the point where the pressure starts to increase; this is consistent with the experiments of Hayashi *et al.*[41] and DNS studies of Volpiani *et al.*[42] It then increases sharply in the interaction and attains a peak value close to the shock-impingement point, followed by a monotonic decrease further downstream. The difference between the two cases is mainly reflected by the larger amplitude of C_h occurring at $(x - x_s)/\delta > 0$ when the interaction strength is increased. This phenomenon is mostly related to the amplified large-scale structures [see Fig. 9(b)], and this will be quantitatively analyzed in Sec. III E.

To characterize the effect of the interaction strength on the recovery of the mean velocity in the downstream region, in Fig. 11, we compare the van Driest transformed mean streamwise velocity profiles at three streamwise locations (denoted by S1–S3 in Figs. 6 and 7) in the two cases. Here, the local wall units are used, and the law of the wall is also added. This figure shows that the recovery of the velocity profile across the boundary layer is different. It can be seen that a universal linear relationship is rapidly recovered in the inner part for $y^+ < 7$, which matches very well with the linear law of the wall. When observing the log-layer region, we can see that the three profiles for the shock29 case show near collapse of the logarithmic law of the wall for $30 < y^+ < 100$, implying that a local equilibrium is quickly recovered at S1 (just downstream of the interaction) for the weak interaction. However, for the strong interaction, it can be seen from Fig. 11(b) that the velocity profile at S1 experiences a characteristic tip, as previously observed by Wu and Martin[23] in a compression ramp and by Pirozzoli and Gross[25] in a reflected shock interaction; good collapse in the log-law region is only obtained at S2–S3. It is suggested that the recovery of the mean velocity in the log-layer region is notably decelerated by the increased interaction strength. In the wake layer, all the velocity profiles show an overshoot over the upstream value; this is remarkably higher for the shock33.2 case, indicating that the recovery in the outer region is uncompleted for both cases.

B. Turbulence evolution

The evolution of turbulence in the downstream region can be identified by comparing the profiles of four components of the Reynolds stress tensor in the wall-normal direction at various streamwise locations, as displayed in Fig. 12 for the two cases. Clearly, this figure highlights substantially different recovery of the Reynolds stresses downstream of the interaction. It is expected that the Reynolds stress components for the shock29 case (dashed lines) experience a rather quick recovery, exhibiting close similarities with the upstream boundary layer; conversely, all the stress components for the shock33.2 case (solid lines) are significantly amplified, and they deviate

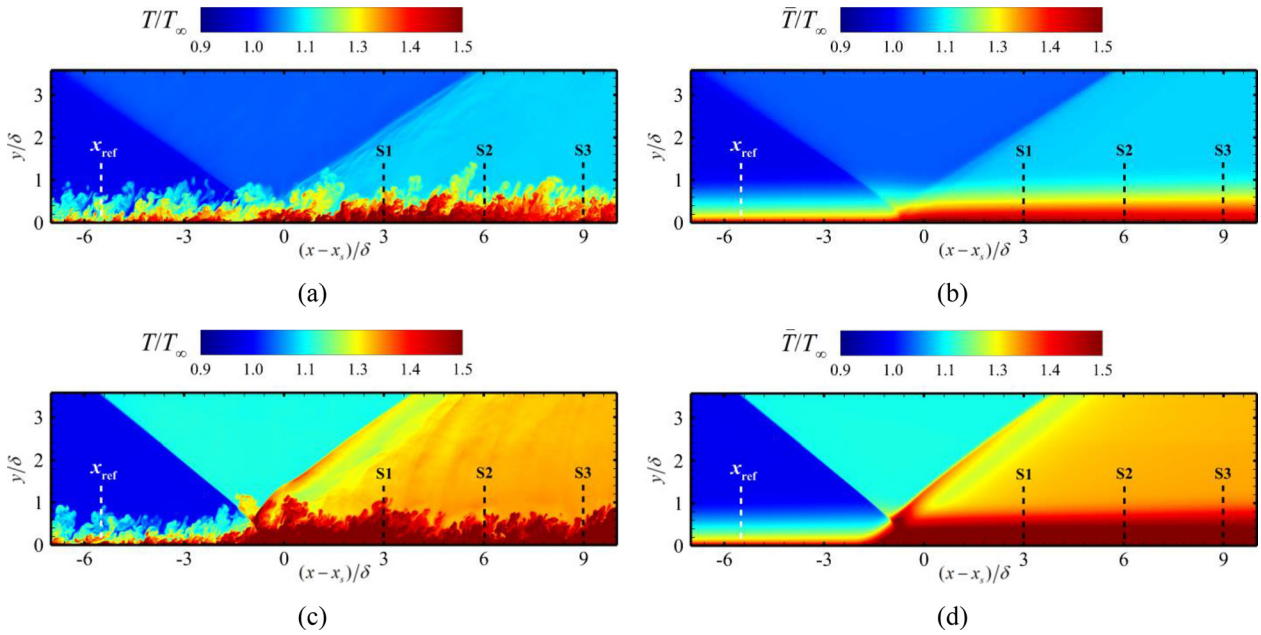

FIG. 6. Contours of (a) and (c) instantaneous and (b) and (d) mean temperature fields in the x–y plane at $z = 0$. (a) and (b): shock29. (c) and (d): shock33.2. S1–S3: $(x - x_s)/\delta = 3$, 6, and 9.

significantly from the upstream profiles, especially in the outer region. Specifically, it can be seen from Fig. 12(a) that the Reynolds normal stress in the weak interaction collapses well in the near-wall region, with the peak value being relatively lower than the maximum peak value at x_{ref}, and only small differences are observed in the region $y^+ > 100$, where the values become slightly higher than the undisturbed values. However, the Reynolds normal stress in the strong interaction is characterized by an inner peak and an outer peak. As the flow

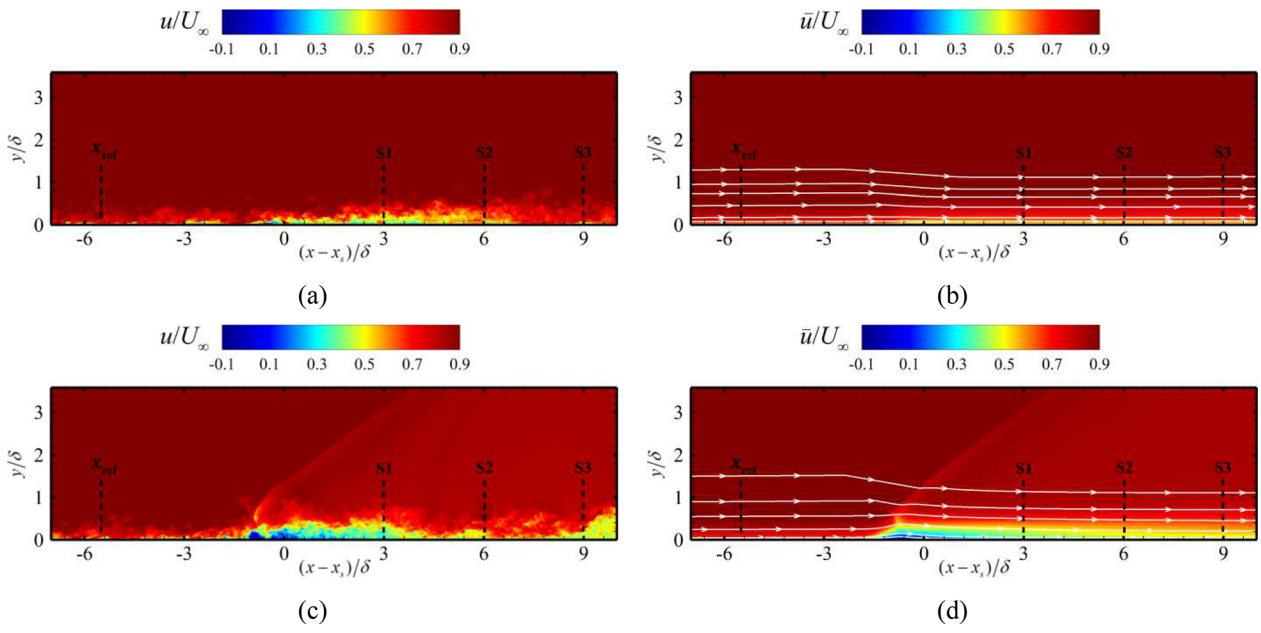

FIG. 7. Contours of (a) and (c) instantaneous and (b) and (d) mean streamwise velocity fields in the x–y plane at $z = 0$ with mean streamlines. (a) and (b): shock29. (c) and (d): shock33.2. S1–S3: $(x - x_s)/\delta = 3$, 6, and 9.

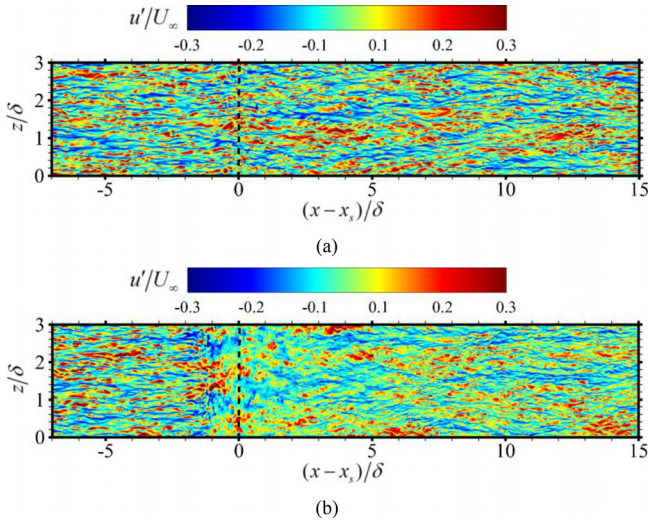

FIG. 8. Contours of streamwise velocity fluctuations in the x–z plane at $y^+ = 8.2$: (a) shock29 and (b) shock33.2. The black dashed lines denote the shock-impingement point at the wall.

recovers further downstream, the dominant outer peak experiences a consistent decrease, whereas the inner peak is continuously increased. As a result, at S3, the inner peak value becomes larger than the outer peak value, suggesting that the Reynolds normal stress is overtaken by the inner peak again. This is the signature of the regenerated near-wall streaks.

In Figs. 12(b)–12(d), we observe that other components of the Reynolds stress tensor for the strong interaction show a similar decreasing trend in the outer region, whereas the components for the weak interaction are slightly changed. It is evident that although the amplified stresses in the outer part of the reattached boundary layer undergo an overall decrease, the peak values are still higher than the upstream values, and the peak locations are consistently moved away from the wall. This phenomenon is probably linked to a continuous spreading of the separated shear layer in the recovery process for the strong interaction with a large separation bubble, as previously reported by Fang *et al.*[27] and Pirozzoli and Gross.[25] It is worth noting that the maximum peak values of the streamwise component at S1–S3 are much lower than that in the incoming flow, as shown in Fig. 12(a), whereas the other components have an overshoot behavior, as shown in Figs. 12(b)–12(d). Consistent with the findings of Fang *et al.*,[27] this is mainly caused by a rapid decay of the streamwise velocity fluctuations in the downstream recovery process; this is because the maximum amplifications of all four components occur in the initial part of the interaction zone (not reported here).

To characterize the effect of the interaction strength on the states of turbulence during the recovery process, turbulent-anisotropy-invariant maps at the selected streamwise locations for the two cases are examined in Figs. 13(a) and 13(b). As suggested by Lumley,[43] the change of anisotropy in the Reynolds stress tensor can be estimated by the anisotropy tensor b_{ij}, which is defined as

$$b_{ij} = \frac{\widetilde{u''_i u''_j}}{\widetilde{u''_k u''_k}} - \frac{1}{3}\delta_{ij}. \tag{7}$$

The turbulence state is characterized by the second (II) and third (III) invariants of b_{ij}, which are written as

$$II = b_{ij}b_{ji}, \quad III = b_{ij}b_{jk}b_{ki}. \tag{8}$$

According to Lumley,[43] the vertices in the anisotropy-invariant map represent a special turbulence state, and all the realizable flows must lie inside the Lumley map. In agreement with previous DNS studies of zero-pressure-gradient TBL by Sun *et al.*[44] and Priebe *et al.*,[45] the computed anisotropy curve at x_{ref} shows a two-component turbulence in the proximity of the wall, caused by the blocking effect, and a maximum anisotropy in the buffer layer at $y^+ = 8.2$, associated with the near-wall streaky structures. As the wall-normal distance increases further, the anisotropy starts to decrease, and turbulence approaches the axisymmetric expansion limit; this is followed by an isotropic state at the outer edge of the boundary layer. In Fig. 13(a), these characteristics are well preserved in the weak interaction, and the computed anisotropy curves at S1–S3 fall close to the upstream curve, aside from a rapid recovery of the decreased maximum anisotropy observed in the near-wall flow.

It can be seen from Fig. 13(b) that the increased interaction strength has a strong influence on the near-wall turbulent state, whereas the paths to the isotropy in the outer region are relatively unaffected. This is consistent with the destruction and regeneration of the alternating near-wall velocity streaks, as previously discussed in Fig. 8(b). At S1, the anisotropy curve, which has drifted away from the one-component limit, is mostly centered in the bottom-left part of the figure; this indicates a considerable decrease in anisotropy in the near-wall turbulence due to the disappearance of the well-organized streaky structures. At S2 and S3, we can see that the near-wall turbulence is dominated by a slow reversal tendency, in which the anisotropy experiences a continuous increase along the two-component limit; this is qualitatively supported by the regenerated streaky structures at $(x - x_s)/\delta > 5$.

Figure 14(a) shows the profiles of TKE $k = {}^1\!/_2\,\widetilde{u''_i u''_i}$ at different streamwise locations for the two cases. It can be seen that for both cases, the TKE in the inner region is lower than that of the upstream TBL, whereas most of turbulence amplification emerges in the outer region $y/\delta > 0.1$ compared to the same locations at x_{ref}. As the interaction strength increases, the downstream TKE becomes smaller in the inner region and larger in the outer region, resulting in an outer peak. In Fig. 14(b), the TKE profiles are re-plotted with local inner scaling to focus on the near-wall asymptotic behavior. It is confirmed that the downstream TKE profiles in both cases satisfy the asymptotic consistency in the viscous sub-layer, where $k^+ \approx A^+ y^{+2}$, but the values of the constant A^+ are different in the two cases. As we can see, collapse of the three TKE profiles for the shock29 cases onto the result at x_{ref} is obtained, suggesting that the value of A^+ is the same as that in the upstream TBL. For the shock33.2 case, it is found that the TKE profile at S1 deviates from the profile at x_{ref} and the differences become negligible as the location is moved downstream, indicating larger values of the constant A^+ in the strong interaction.

The significant terms in the TKE budgets at the selected streamwise locations for the shock29 and shock33.2 cases are reported in Figs. 15(a) and 15(b), respectively, as functions of the normalized wall-normal distance y/δ. As suggested by Pirozzoli *et al.*,[34] the TKE budget equation is as follows:

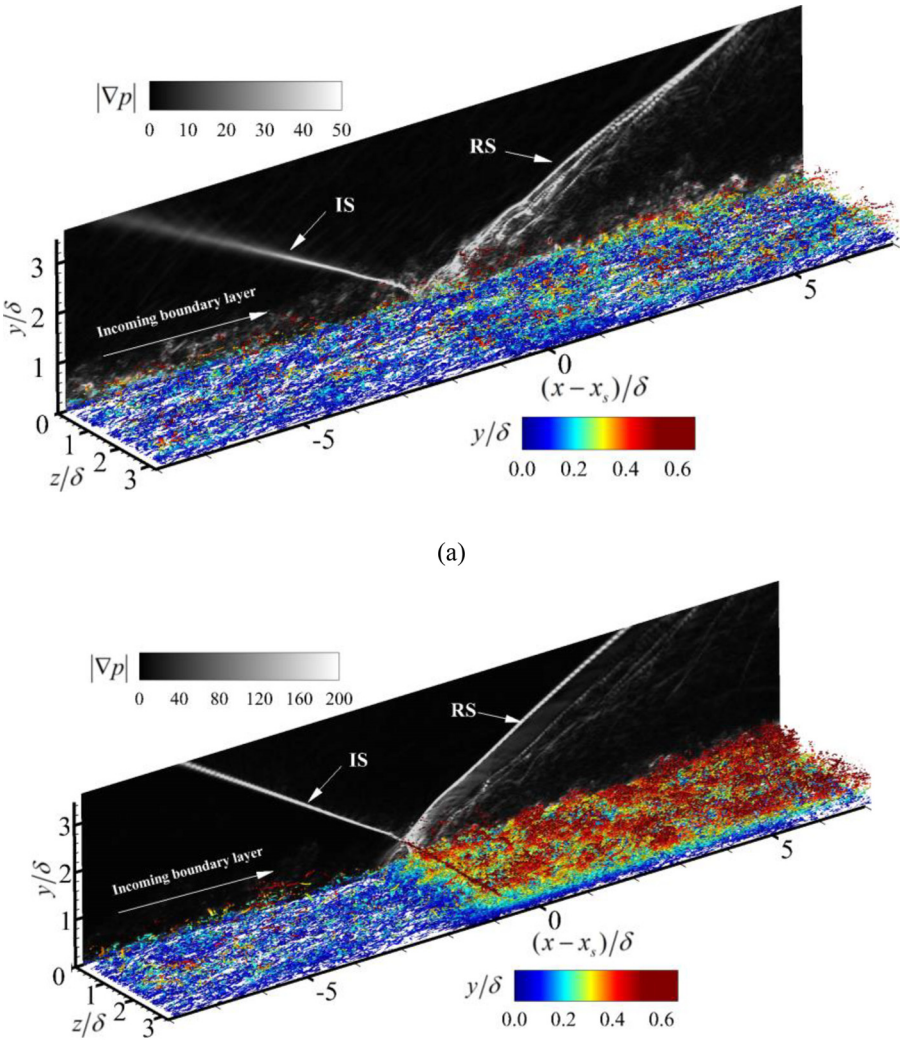

FIG. 9. Iso-surfaces of the Q criterion colored by the wall-normal distance together with the instantaneous pressure gradient modulus $|\nabla p|$ in the x–y plane at $z = 0$: (a) shock29 and (b) shock33.2. IS: incident shock; RS: reflected shock.

$$\frac{\partial \bar{\rho} k}{\partial t} = \underbrace{-\frac{\partial \bar{\rho} \widetilde{u}_j k}{\partial x_j}}_{C_k} \underbrace{-\bar{\rho} \widetilde{u''_i u''_j} \frac{\partial \widetilde{u}_i}{\partial x_j}}_{P_k} + \underbrace{\frac{\partial (\overline{\sigma'_{ij} u''_i})}{\partial x_j}}_{V_k} - \underbrace{\overline{\sigma'_{ij} \frac{\partial u''_i}{\partial x_j}}}_{\Pi_k} \underbrace{-\frac{\partial}{\partial x_j}\left[\frac{1}{2}\bar{\rho} \widetilde{u''_i u''_i} u''_j + \overline{p' u''_j}\right]}_{T_k} + \underbrace{\overline{p' \frac{\partial u''_i}{\partial x_i}} + \bar{u}''_i \left(\frac{\partial \bar{\sigma}_{ij}}{\partial x_j} - \frac{\partial \bar{p}}{\partial x_i}\right)}_{A_k}, \tag{9}$$

where C_k, P_k, V_k, Π_k, T_k, and A_k, respectively, denote the terms of convection, production, viscous diffusion, viscous dissipation, turbulent and pressure transport, and compressibility effect. Note that the two terms C_k and A_k are rather small, and for clarity, they are not shown in the figure.

According to Fig. 15, it is clear that the shock interaction exhibits little influence on the TKE budgets in the recovery process, where all the terms in the two cases have typical behaviors of a zero-pressure-gradient boundary layer flow, consistent with numerical results of Pirozzoli *et al.*[34] and Sun *et al.*[44] Clearly, production balances dissipation over most of the boundary layer, whereas the TKE is transported toward the wall by turbulent and pressure transport and viscous diffusion. In the proximity of the wall, the production is negligible, and the balance between dissipation and viscous diffusion is more prominent. It is important to note, however, that the distribution of the production term is essentially affected by the increased interaction strength. In Fig. 15(a), the production profiles at S1–S3 show good collapse in the weak interaction, peaking at $y^+ \approx 10$ and exhibiting a similar trend to that at x_{ref}. In contrast to this, despite the production still attaining its maximum value in the near-wall region, a wall-detached production peak is visible at $y^+ \approx 300$–400, as also described by Pirozzoli *et al.*[46] During the recovery process, we observe that the peak value in

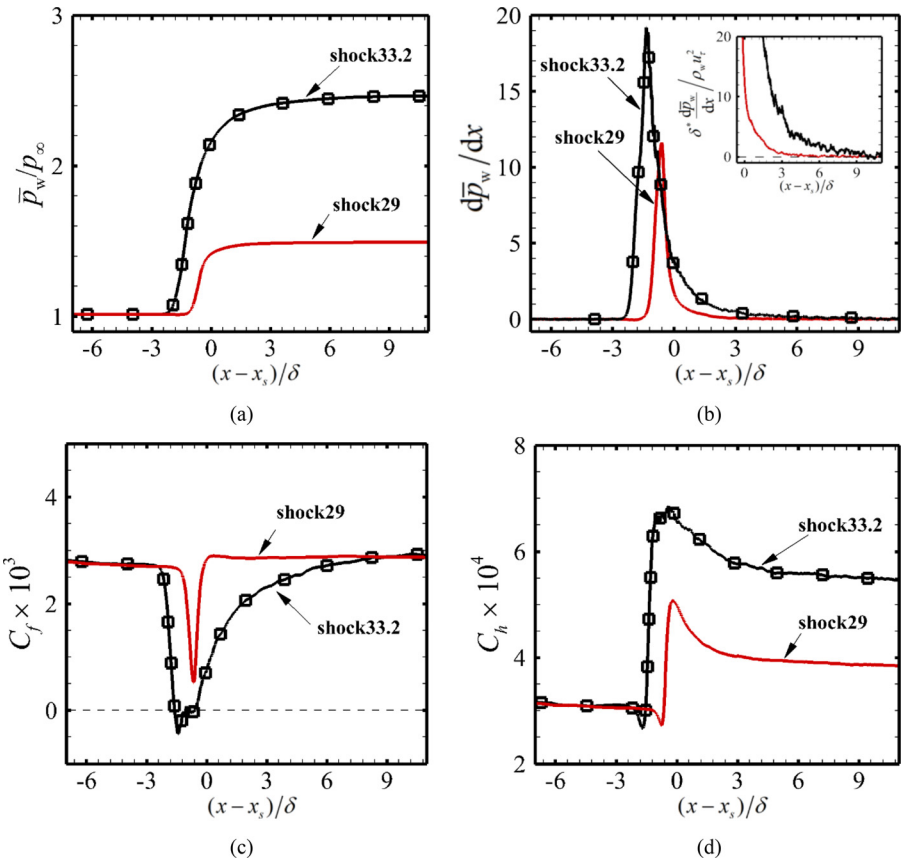

FIG. 10. Effect of interaction strength on mean wall quantities: (a) pressure $\bar{p}_w$; (b) pressure gradient $d\bar{p}_w/dx$; (c) skin friction coefficient C_f; and (d) heat flux C_h.

the near-wall region experiences a significant increase, close to the upstream value at x_{ref}, whereas the magnitude of the outer peak is slightly decreased. It is reasonable to infer that the mechanism of turbulent production across the entire boundary layer is different downstream of the interaction in the two cases.

As a further investigation of turbulence production throughout the boundary layer, the local contribution to the production of turbulence at a given wall-normal location (i.e., $P_k dy+$) is analyzed by plotting the product y^+P_k as a function of y^+ in logarithmic scale. This is because $y^+P_k d(\log y^+)$ is mathematically equivalent to $P_k dy^+$, and the area below the y^+P_k curve represents the integral contribution to the total turbulence production, as suggested by Wu *et al.*[47] The premultiplied plots for the weak and strong interactions are given in Figs. 16(a) and 16(b), respectively.

It is confirmed that with increasing interaction strength, the area in the outer region increases dramatically, suggesting that the outer

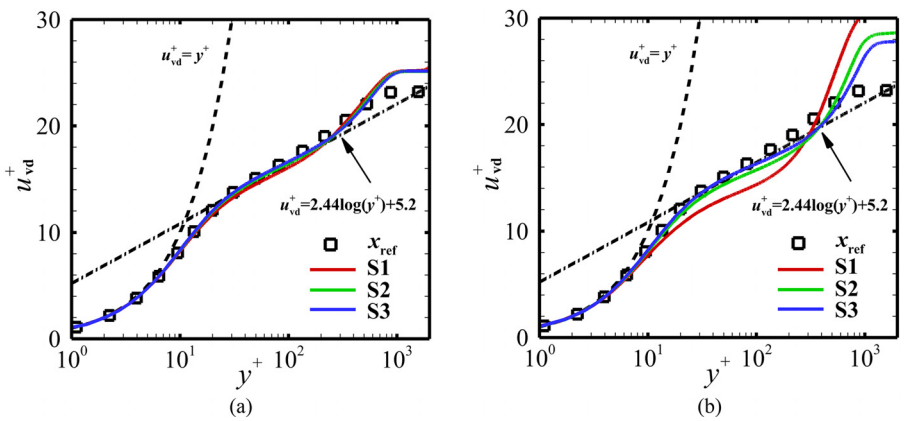

FIG. 11. Profiles of the van Driest transformed mean streamwise velocity at different streamwise locations: (a) shock29 and (b) shock33.2.

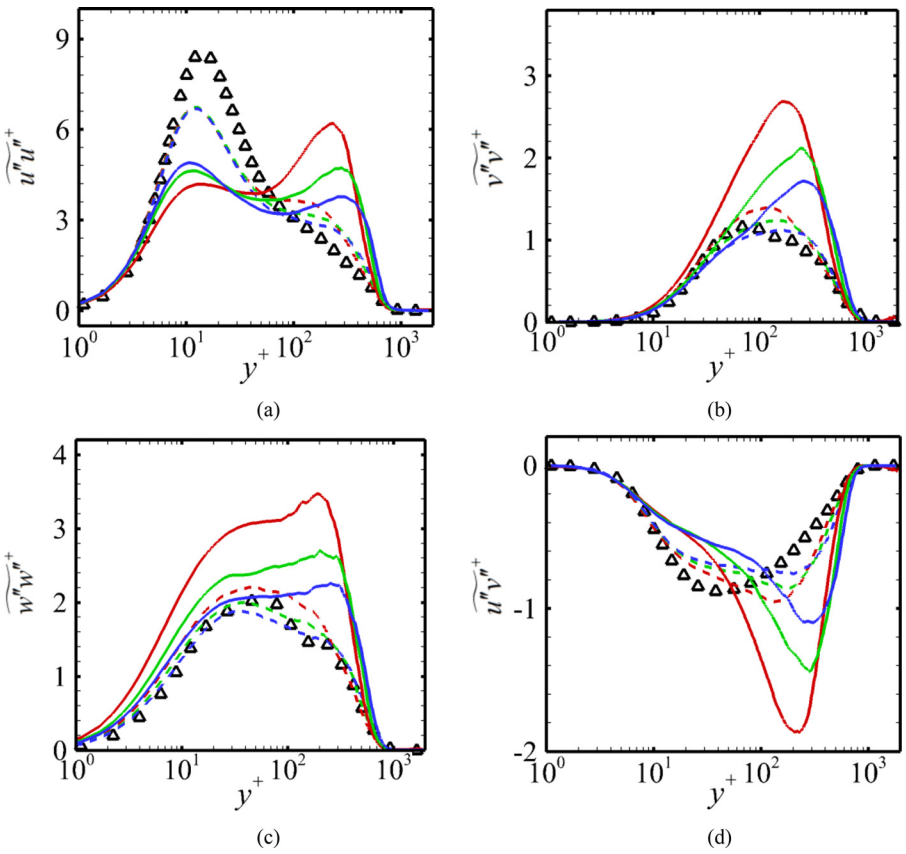

FIG. 12. Profiles of the Reynolds stress components at different streamwise locations for the shock29 (dashed lines) and shock33.2 (solid lines) cases: (a) $\widetilde{u''u''}^+$, (b) $\widetilde{v''v''}^+$, (c) $\widetilde{w''w''}^+$, and (d) $\widetilde{u''v''}^+$. Triangles: x_{ref}; red: S1; green: S2; blue: S3.

region contributes the most significant part of the turbulence production inside the boundary layer. This can be better quantified by comparing the proportion of the area at $y^+ > 100$ to the total area. Specifically, at x_{ref}, the outer region only carries about 30% of the total turbulence production, implying that most of the turbulence is produced in the near-wall region of the upstream TBL. Downstream of the interaction, the increasingly pronounced contributions in the shock33.2 case are about 82%, 74%, and 66% for the three locations S1–S3, respectively, much larger than the corresponding values of about 47%, 45%, and 43% in the shock29 case. This quantitatively demonstrates the importance of the outer layer in the strong interaction.

To examine in depth the contribution at a given wall-normal location and at a given spanwise scale, we have analyzed $k_z^+ y^+ \Phi_P$ in the ($\log_{10}\lambda_z^+$, $\log_{10} y^+$) plane at S3 (the other locations being similar and, thus, not shown) for the two cases. These are shown in

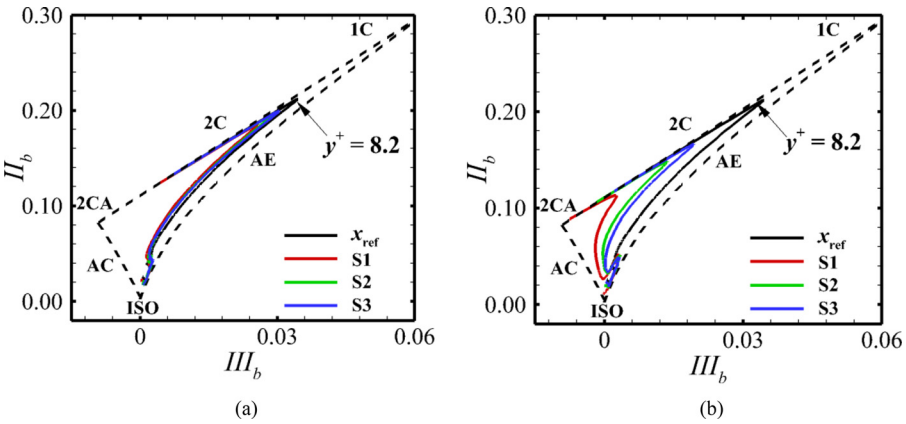

FIG. 13. Reynolds-stress anisotropy-invariant maps at different streamwise locations: (a) shock29 and (b) shock33.2. 1C: one-component; 2C: two-components; 2CA: two-components axisymmetric; AE: axisymmetric expansion; ISO: isotropic; AC: axisymmetric compression.

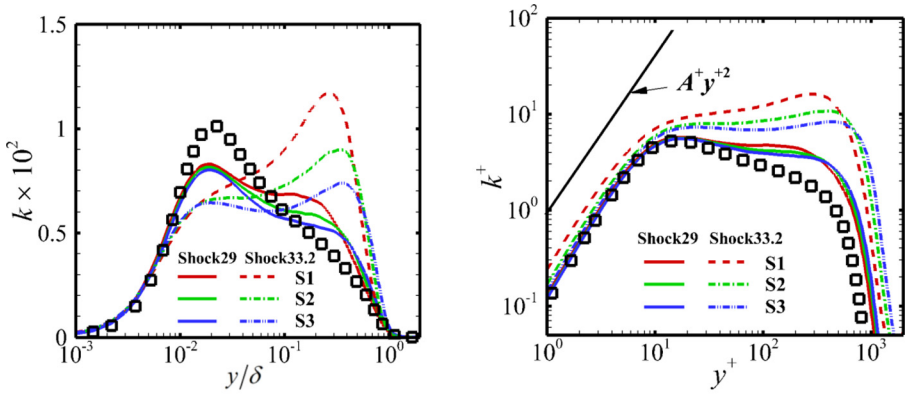

FIG. 14. Profiles of TKE in (a) outer scaling and (b) local inner scaling at different streamwise locations. Squares represent the data at x_{ref}.

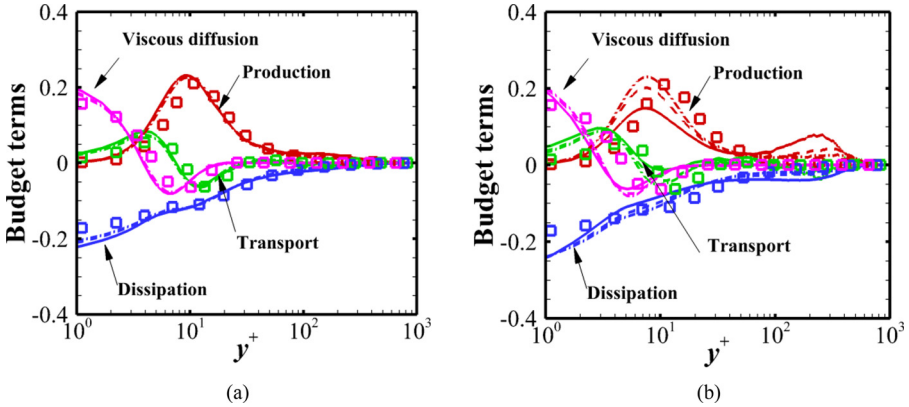

FIG. 15. TKE budget profiles at the three streamwise locations for the (a) shock29 and (b) shock33.2 cases. Squares represent the data at x_{ref}. Solid lines: S1; dashed lines: S2; dash-dotted lines: S3.

Figs. 15(c) and 15(d), where k_z^+ and λ_z^+ represent the spanwise wavenumber and wavelength, respectively, and Φ_P denotes the spanwise spectrum of the production term P_k. According to Fig. 15(c), it can be seen that the most significant contribution in the weak interaction comes from the inner region at $y^+ \approx 10$ and $\lambda_z^+ \approx 100$, supporting the understanding that the near-wall low-speed streaks dominate the turbulence production in the recovery process of the weak interaction [see the velocity fluctuations in Fig. 8(a)]. Clearly, the influence of the shock interaction is mainly reflected by the emergence of a second outer spectral peak with a very small value, suggesting that the shock interaction also increases the local contribution of the outer large-scale structures. As the interaction strength increases, Fig. 15(d) highlights that the value of the outer spectral peak at $y^+ \approx 363$ and $\lambda_z^+ \approx 478$ becomes much larger than that of the inner spectral peak, which is consistent with the qualitative observations in Fig. 9(b). Therefore, we believe that the enhanced contribution of the outer large-scale structures in the shock33.2 case overrides that of the inner small-scale structures, and the outer large-scale structures become apparently dominant.

C. Wall pressure fluctuations

The instantaneous pressure fluctuations in the wall plane for the two cases are reported in Figs. 17(a) and 17(b). The influence of the interaction strength on the amplitude and structure of the wall pressure fluctuation field is apparent, with the strong interaction inducing higher amplitudes and larger characteristic length scales of wall pressure fluctuations. When the interaction strength is increased, the pressure fluctuations experience a significant amplification in the separation region [see the zone $-2 < (x - x_s)/\delta < 0$], and larger pressure-carrying structures are frequently observed starting at the shock-impingement point and becoming dominant in the downstream relaxation region. The increased length scales will be better quantified in the two-point correlation maps presented later.

According to Fig. 17(c), upstream of the interaction, the rms value of wall pressure fluctuations has a constant value of $p_{w,rms} = 0.025p_\infty$, corresponding to $p_{w,rms}/\tau_w = 2.57$ (τ_w being the mean wall shear stress), which is comparable to the value of $p_{w,rms}/\tau_w = 2.8$ given by the DNS of Duan *et al.*[30] for a spatially developed Mach 5.86 turbulent boundary layer at $Re_\tau = 453.1$ and $T_w/T_r = 0.76$. For the weak interaction, $p_{w,rms}/p_\infty$ attains a peak value of 0.055 at $(x - x_s)/\delta \approx -0.38$, whereas the maximum of $p_{w,rms}/p_\infty$ for the strong interaction, located at $(x - x_s)/\delta \approx -1$, is nearly 3.5 times the upstream value. Downstream of the interaction, the magnitude of $p_{w,rms}/p_\infty$ for both cases exhibits a continuous decrease, approaching a nearly constant level at the end of the recovery process. It is found that $p_{w,rms}/p_\infty = 0.056$ for the shock33.2 case at $(x - x_s)/\delta \approx 9$ and $p_{w,rms}/p_\infty = 0.033$ for the shock29 case, both larger than the value in the

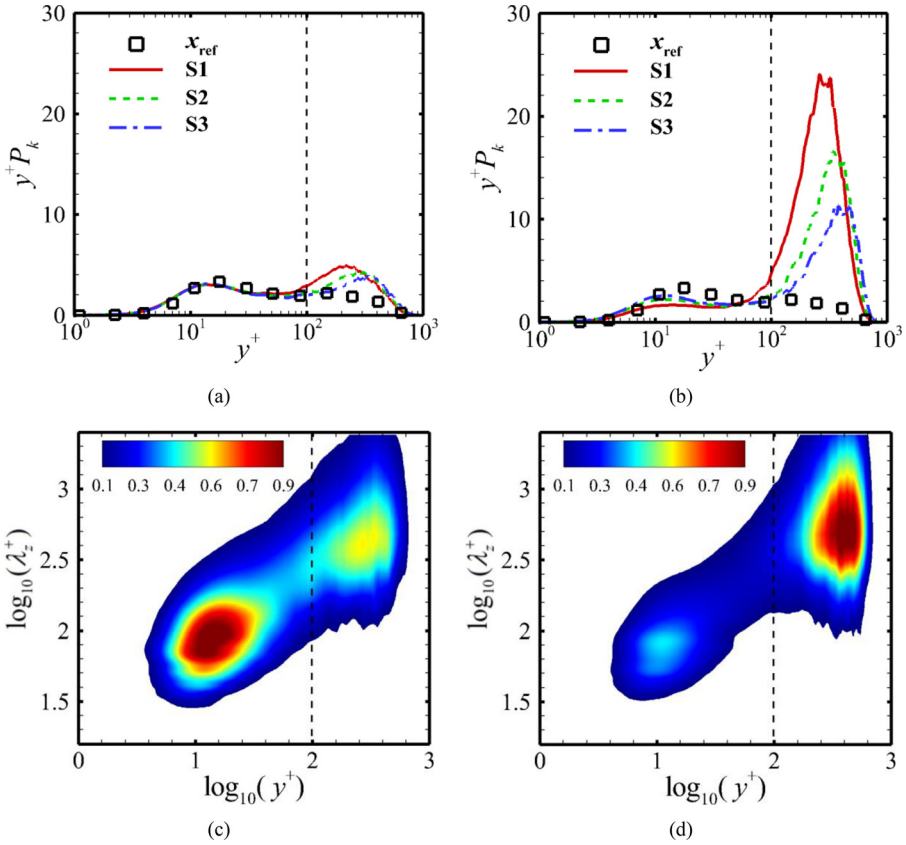

FIG. 16. Profiles of the pre-multiplied turbulence production (a) and (b) and their spanwise energy spectra (c) and (d) for the shock29 (left panels) and shock33.2 (right panels) cases. The spectra in (c) and (d) are normalized by their maximum values.

upstream TBL. This means that the recovery of the dynamic pressure is not yet completed for the two cases. As shown in Fig. 17(d), approximate collapse of the rms value of wall pressure fluctuations for the two cases is found at $(x - x_s)/\delta > 6$ when data are scaled with respect to the local mean wall pressure.

The probability density functions (PDFs) of wall pressure fluctuations at different streamwise locations are reported in Fig. 18(a) on a linear scale and in Fig. 18(b) on a logarithmic scale. It can be seen that the PDFs in the recovery process are weakly dependent on the interaction strength when the local rms value is used for normalization. A standard Gaussian distribution is also included in this figure for comparison. As shown in Fig. 18(a), all the PDFs are nearly symmetric, having a similar shape to the Gaussian distribution, but their peak values are larger than that of the Gaussian distribution. In Fig. 18(b), it is confirmed that the tails of the normalized PDFs show a satisfactory collapse, aside from slight differences at extreme pressure fluctuations. Such a behavior has been recently observed in the normalized PDFs of wall heat flux fluctuations in the DNS of Tong *et al.*[15] for a supersonic SWTBLI.

To characterize the influence of the interaction strength on the variations of energy distribution among different frequencies, Fig. 19(a) shows the pre-multiplied pressure spectra $f\Phi$ as a function of the scaled frequency $f\delta/U_\infty$ at different streamwise locations. In this figure, the spectra are normalized by the square of the local rms value of wall pressure fluctuation, $p_{w,rms}$. At x_{ref}, it can be seen that the dominant bump in the pressure spectrum is centered at $f\delta/U_\infty \approx 1.0$, which is consistent with the characteristic frequency of the most energetic structures found in previous experiments and simulations of zero-pressure-gradient compressible TBLs.

For both the shock29 and shock33.2 cases, we observe that the normalized spectra at S1–S3 exhibit approximate collapse. The spectral density is slightly changed by the weak interaction, whereas the strong interaction shifts the broadband peak of the spectrum to intermediate frequencies $0.3 < f\delta/U_\infty < 1.0$, implying that the characteristic frequencies in the shock33.2 case are lower than those in the shock29 case. The reduction of the dominant frequencies between the two cases is mainly caused by the combined effects of the increase in the boundary layer thickness and the decrease in convection velocity in the downstream relaxation region. In Fig. 19(b), a quantitative comparison of the pressure spectra for the two cases is reported; here, the integration of the power spectral density Φ below a certain frequency ζ is performed. For the frequency range $f\delta/U_\infty < 1.0$, the portion of the fluctuating energy at x_{ref} is about 43%, and this increases to approximately 51% and 82% at S1–S3 for the weak and strong interactions, respectively.

To characterize the spatial and temporal properties of the wall pressure fluctuations during the recovery process, we analyzed the two-point spatial correlation coefficient $R_{pp}(\Delta x^+, \Delta z^+, 0)$ and the longitudinal space–time correlation coefficient $R_{pp}(\Delta x^+, 0, \Delta t^+)$ at different streamwise locations, as shown in Figs. 20 and 21, respectively.

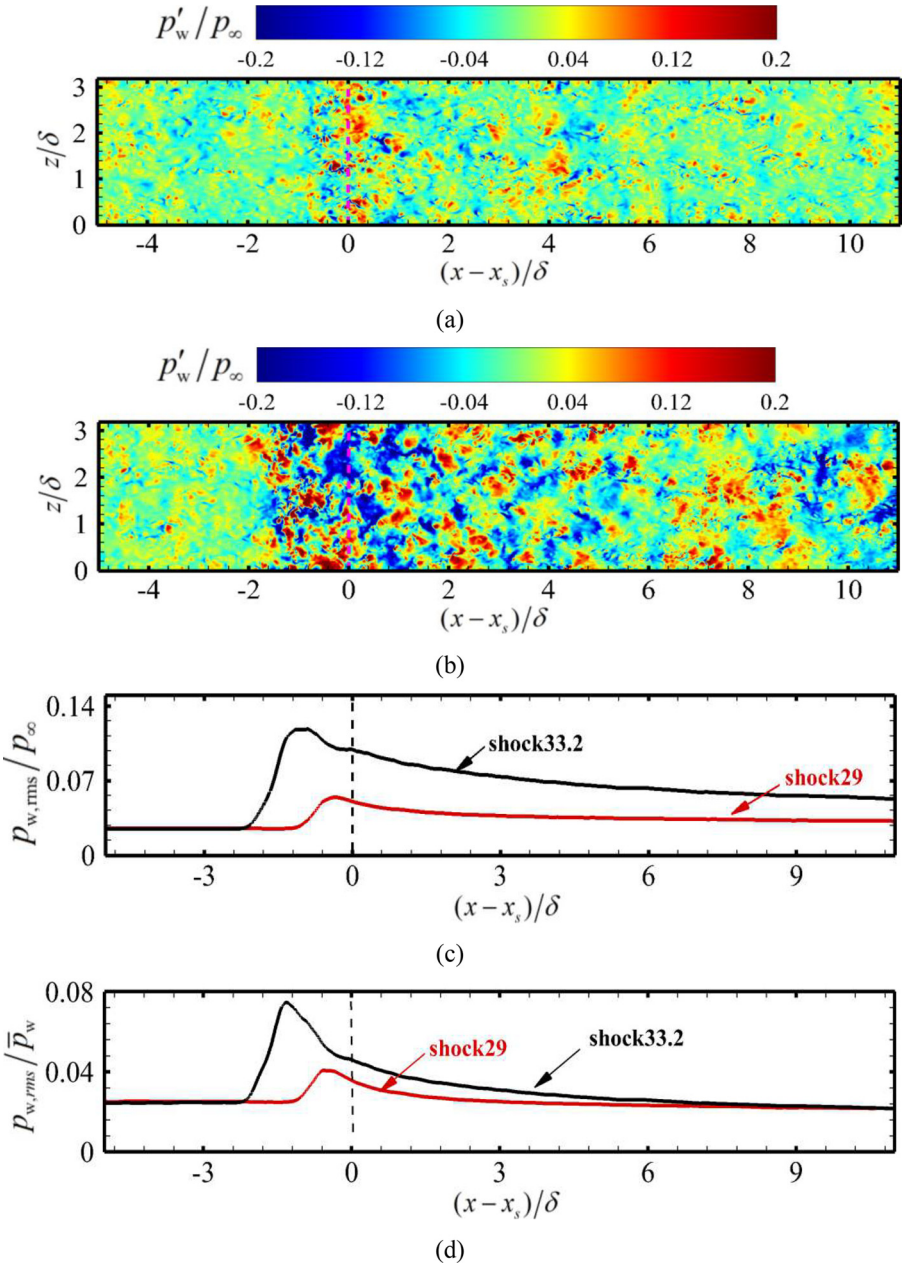

FIG. 17. Contours of instantaneous wall pressure fluctuations for the two cases: (a) shock29 and (b) shock33.2. Streamwise evolution of the normalized rms wall pressure fluctuations: (c) free-stream pressure p_∞ and (d) local mean wall pressure $\bar{p}_w$. The dashed lines in (c) and (d) denote the nominal impingement point.

Following Bernardini and Pirozzoli,[48] the correlation coefficient $R_{pp}(\Delta x^+, \Delta z^+, \Delta t^+)$ of wall pressure is defined as

$$R_{pp}(\Delta x^+, \Delta z^+, \Delta t^+) = \frac{\overline{p'(x_0, z, t)p'(x_0 + \Delta x^+, z + \Delta z^+, t + \Delta t^+)}}{\sqrt{\overline{p'(x_0, z, t)^2}}\sqrt{\overline{p'(x_0 + \Delta x^+, z + \Delta z^+, t + \Delta t^+)^2}}}, \quad (10)$$

where x_0 denotes the reference probe, Δx^+ and Δz^+ are the streamwise and spanwise spatial separations, respectively, and Δt^+ denotes the time delay.

In Fig. 20(a), the correlation map in the upstream TBL (x_{ref}) exhibits a typical shape also observed in previous studies of low-speed and compressible wall-bounded flows,[48,49] with a roughly circular pattern at small separations and a spanwise elongated behavior at large separations; these are the remnants of the near-isotropic nature of the small-scale pressure structures and the anisotropic nature of the large-scale pressure structures, respectively. Observing Figs. 20(b)–20(d), we remark that a similar pattern is observed downstream of the interaction for the two cases, supporting the qualitative observations in Fig. 17. However, in Fig. 20(b), the spatial extents of the correlation maps for the two cases experience a considerable increase at S1, which

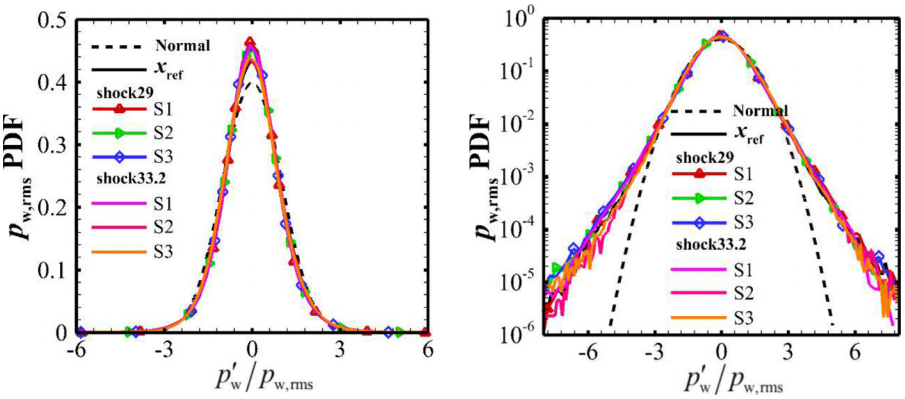

FIG. 18. Normalized PDFs of wall pressure fluctuations at different streamwise locations for the two cases plotted on (a) a linear scale and (b) a logarithmic scale.

is remarkably higher for the strong interaction (see the iso-lines). Taking the correlation level of 0.3 as an example, the extents in the x and z directions are about $\Delta x^+ = 126$ and $\Delta z^+ = 150$ at x_{ref}, respectively. For the shock33.2 case, the spatial extents are increased to $\Delta x^+ = 304$ and $\Delta z^+ = 412$, compared to $\Delta x^+ = 162$ and $\Delta z^+ = 218$ for the shock29 case. As the probe moves downstream, a different recovery behavior is found in the dimensions of the correlation structures. It is clearly seen from Figs. 20(c) and 20(d) that the dimensions of the iso-contours in both the streamwise and spanwise directions are slightly changed at S2 and S3 when the interaction is weak, while the spatial extents of the iso-lines experience an obvious increase in the strong interaction. For example, the streamwise and spanwise length scales for the correlation level of 0.3 in the shock33.2 case are both approximately 15% larger than those at S1. Although the reason for this is not clear, it might be related to the enhanced large-scale structures in the outer region of the reattached boundary layer, as previously observed in Fig. 9. In Fig. 21, the maps of the space–time correlation coefficient $R_{pp}(\Delta x^+, 0, \Delta t^+)$ for the two cases show a narrowed forward-leaning behavior in the Δt^+–Δx^+ plane at all streamwise locations, implying the downstream propagation of the pressure fluctuations in the relaxation region. Clearly, two important observations are obtained regarding the influence of the interaction strength on the spatial and temporal coherences. First, the extents of the correlation maps at S1–S3 increase significantly in both time and the streamwise direction; this is very similar to the space–time correlations of wall pressure fluctuations reported by Bernardini *et al.*[50] in a transonic-shock/boundary-layer interaction. Specifically, the spatial extent for the correlation level of 0.3 are increased from $\Delta x^+ = 424$ at x_{ref} to $\Delta x^+ = 691$ at S3 for the shock29 case and $\Delta x^+ = 1332$ at S3 for the shock33.2 case. The temporal extent at x_{ref} is $\Delta t^+ = 21$, and the corresponding values at S3 in the two cases are $\Delta t^+ = 36$ and $\Delta t^+ = 74$, respectively. Second, the inclination angle between the major axis of the correlation map and the axis of the delay time is essentially changed downstream of the interaction, where an overall decrease in the inclination angle is observed in the strong interaction, which indicates a substantial reduction of the convection velocity in the shock33.2 case.

Figures 22(a) and 22(b) show the convection velocity U_c/U_∞ as a function of time delay Δt^+ at different streamwise locations for the weak and strong interactions, respectively. Similar to the results of Duan *et al.*[30] and Bernardini *et al.*,[48] the convection velocity of wall pressure fluctuations for a given time delay Δt^+ is calculated as the ratio $\Delta x^+/\Delta t^+$, where the value of Δx^+ is selected as

$$\left.\frac{\partial R_{pp}(r_x, 0, \Delta t^+)}{\partial r_x}\right|_{r_x=\Delta x^+} = 0. \tag{11}$$

In both Figs. 22(a) and 22(b), the computed convection velocity at x_{ref} is also added for direct comparison. It is apparent that both the shock interactions exert a significant influence on the convection speed of the wall pressure fluctuations. Upstream of the interaction, the

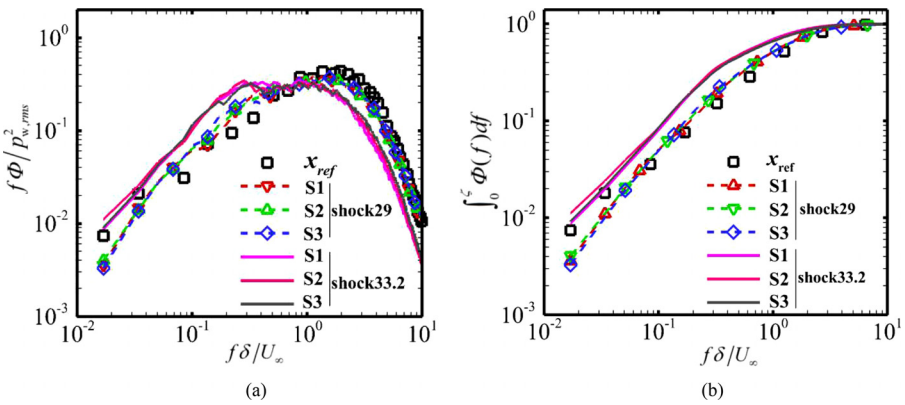

FIG. 19. (a) Pre-multiplied wall pressure spectra and (b) integration of wall pressure spectra at different streamwise locations for the two cases.

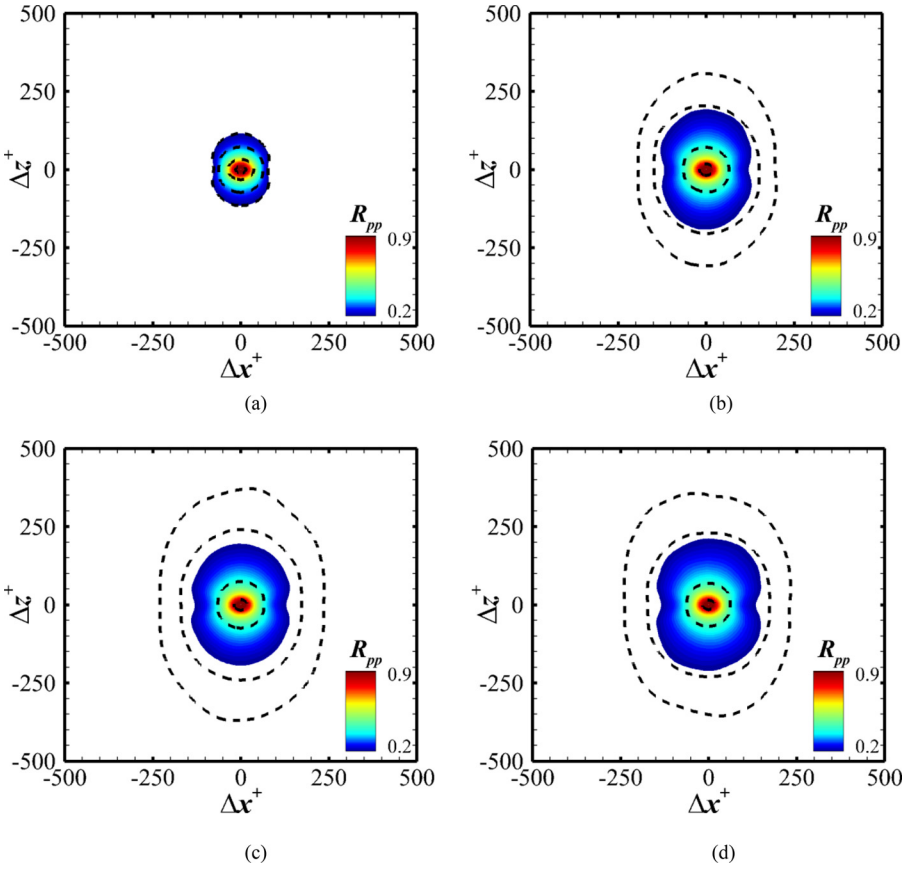

FIG. 20. Two-point pressure-correlation maps in the wall plane, $R_{pp}(\Delta x^+, \Delta z^+, 0)$, for the shock29 (contours) and shock33.2 (iso-lines) cases. (a) x_{ref}; (b) S1; (c) S2; (d) S3. Four black iso-lines, $R_{pp} = 0.2$, 0.3, 0.6, and 0.9, are shown in the shock33.2 case.

propagation of fluctuations is strongly dependent on the time delay, i.e., a larger time delay results in a larger convection velocity; this is consistent with the measured and computed results in canonical incompressible and compressible boundary layers.[30,51] At x_{ref}, the convection velocity is estimated as $U_c \approx 0.55\,U_\infty$ at a small time delay (associated with small-scale fluctuations) and as $U_c \approx 0.75\,U_\infty$ at a large time delay (associated with large-scale fluctuations).

For the two flow cases considered, it is emphasized that the overall trend of the convection velocity is well preserved in the recovery process, but the fluctuations propagate downstream much more slowly than those in the upstream TBL. When the interaction is weak, the results in Fig. 22(a) show that the convection velocities at S1–S3 collapse well onto each other, ranging from $0.45\,U_\infty$ to $0.7\,U_\infty$. However, it is apparent from Fig. 22(b) that the convection velocity exhibits a reversal tendency in the strong interaction. Clearly, it first drops to $0.35 < U_c/U_\infty < 0.55$ at S1, and it then increases at S2 and S3, attaining values in the range $0.4\,U_\infty$–$0.6U_\infty$. It is suggested that the increased interaction strength leads to a much smaller convection velocity of wall pressure fluctuations in the downstream relaxation region. We also find that the local mean velocity becomes much smaller in the two cases after the flow passes through the interaction, with a good collapse of the velocity profiles in the shock29 case and a reversal tendency of those in the shock33.2 case (not shown here). This is very similar to the results discussed in Fig. 22; furthermore, the wall pressure fluctuations are strongly dependent on a multi-scale structure across the whole boundary layer, and this is found to propagate downstream at a value close to the local mean streamwise velocity, as reported by Duan *et al.*[30] and Bernardini and Pirozzoli.[48] In view of this, it is hypothesized that the different recovery of the decreased convection velocity could probably be linked to the change of the mean streamwise velocity profile in the downstream region.

D. Mean skin friction decomposition

In this section, we aim to quantify the mean skin friction generation in the relaxation region through the decomposition method proposed by Renard and Deck[52] and Li *et al.*[12] Here, the mean skin friction C_f, defined as $C_f = 2(\mu\partial\bar{u}/\partial y)_w/\rho_\infty u_\infty^2$, is decomposed as

$$C_f = \underbrace{\frac{2}{\rho_\infty u_\infty^3}\int_0^\infty \bar{\tau}_{yx}\frac{\partial\widetilde{u}}{\partial y}\mathrm{d}y}_{C_{f,\mathrm{V}}} + \underbrace{\frac{2}{\rho_\infty u_\infty^3}\int_0^\infty \bar{\rho}\left(-\widetilde{u''v''}\right)\frac{\partial\widetilde{u}}{\partial y}\mathrm{d}y}_{C_{f,T}} + \underbrace{\frac{2}{\rho_\infty u_\infty^3}\int_0^\infty (\widetilde{u}-u_\infty)\left[\bar{\rho}\left(\widetilde{u}\frac{\partial\widetilde{u}}{\partial x}+\widetilde{v}\frac{\partial\widetilde{u}}{\partial y}\right)+\frac{\partial}{\partial x}\left(\bar{\rho}\widetilde{u''u''}-\bar{\tau}_{xx}\right)+\frac{\partial\bar{p}}{\partial x}\right]\mathrm{d}y}_{C_{f,G}}, \tag{12}$$

where $C_{f,V}$, $C_{f,T}$, and $C_{f,G}$, respectively, represent the direct effect of viscous dissipation, the power spent for the TKE production, and the

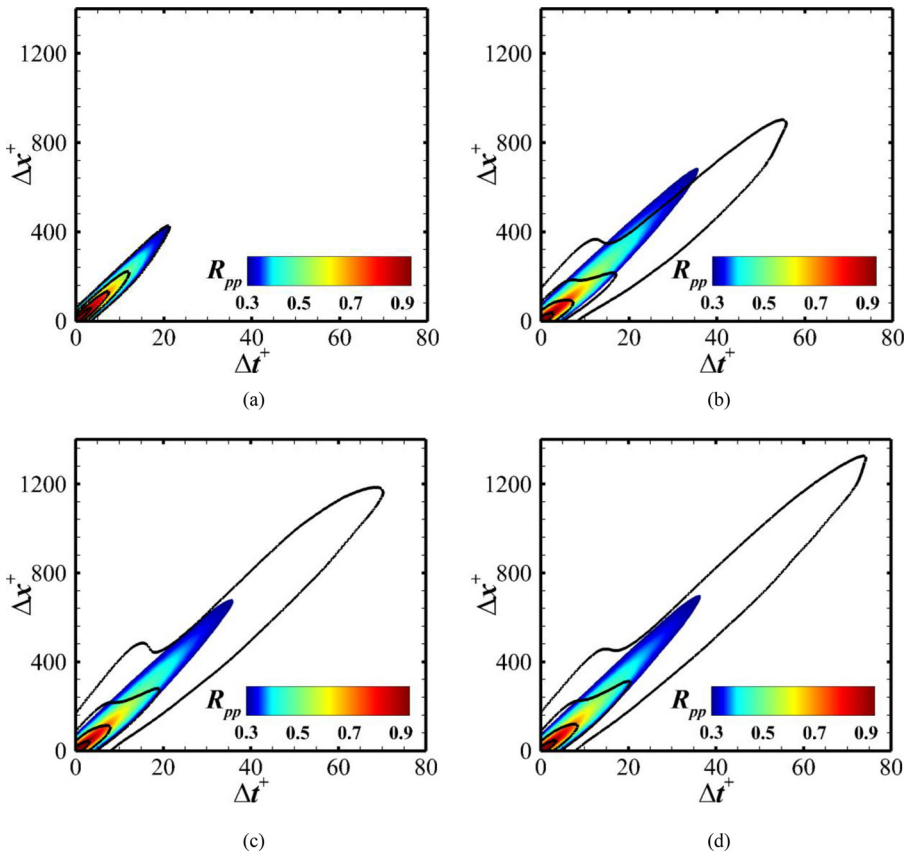

FIG. 21. Space–time correlation maps $R_{pp}(\Delta x^+, 0, \Delta t^+)$ of wall pressure at different streamwise locations for the shock29 (contours) and shock33.2 (iso-lines) cases: (a) x_{ref}; (b) S1; (c) S2; and (d) S3. Four black iso-lines, $R_{pp} = 0.3$, 0.5, 0.7, and 0.9, are shown in the shock33.2 case.

spatial growth of the flow. The variables $\bar{\tau}_{xx}$ and $\bar{\tau}_{yx}$ are the streamwise components of the mean shear and normal stress, respectively.

Figure 23 shows a comparison of the decomposed contributions to the mean skin friction C_f at different streamwise locations. For the two cases, the relative errors, defined as $[C_{f,\mathrm{V}} + C_{f,\mathrm{T}} + C_{f,\mathrm{G}} - C_f]/C_f$, are confined within $\pm 0.3\%$, demonstrating that the forthcoming decomposition analysis is reliable. We remark that the generation of C_f in both the weak and strong interactions is dominated by a large positive contribution of $C_{f,\mathrm{T}}$. Interestingly, the positive contributions of $C_{f,\mathrm{T}}$ at S1 and S2 for the shock33.2 case are 164.76% and 104.13%, respectively, meaning that the positive $C_{f,\mathrm{T}}$ is even larger than the local C_f. Such a behavior is not observed in the shock29 case, where the $C_{f,\mathrm{T}}$ contribution is less than 59% at all streamwise locations. It is apparent that the overshoot of the positive $C_{f,\mathrm{T}}$. is balanced by the large negative contribution of $C_{f,\mathrm{G}}$ in the strong interaction, which is about -87.7% and -30.88% at S1 and S2, respectively, whereas the contributions of $C_{f,\mathrm{G}}$ at all streamwise locations in the weak interaction are always positive and can be neglected due to their small magnitude. These trends

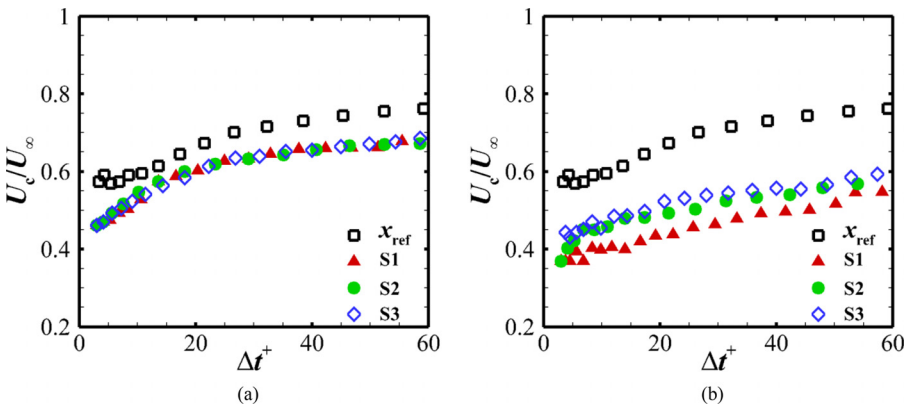

FIG. 22. Local convection velocity U_c/U_∞ as a function of time delay Δt^+: (a) shock29 and (b) shock33.2.

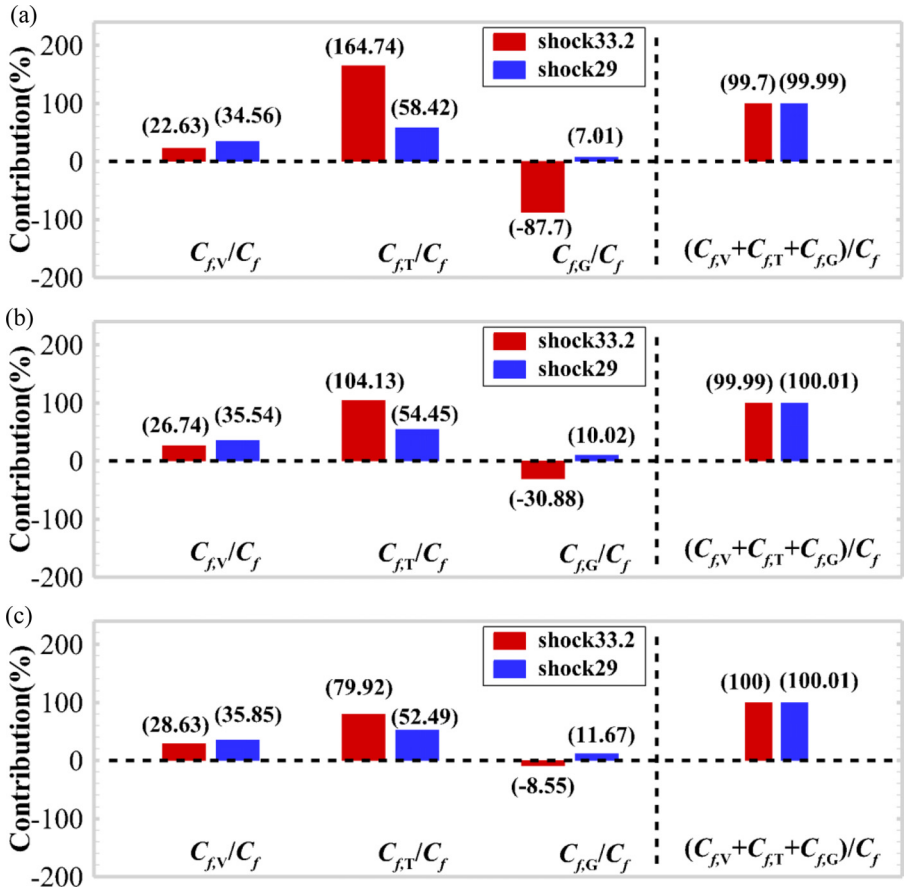

FIG. 23. Contributions to C_f at different streamwise locations: (a) S1; (b) S2; (c) S3.

suggest that the C_f generation in the initial region of the downstream recovery process is essentially changed by the strong interaction. Furthermore, a direct comparison of the three terms in the contribution of $C_{f,G}$ reveals that the negative $C_{f,G}$ is caused by the streamwise gradient of mean pressure in the strong interaction; this is very similar to the decomposed results of the mean skin friction in adverse-pressure-gradient TBLs reported by Fan *et al.*[53] It can be also seen from Fig. 23(c) that the $C_{f,T}$ contribution at S3 increases as the interaction strength increases, since the magnitudes of the local C_f in the present two cases are nearly the same.

In Fig. 24, we report the pre-multiplied integrand of $C_{f,T}/C_f$ as a function of the wall-normal distance y^+ to give a better understanding of the mean skin friction generation in the two cases. Regarding the $C_{f,T}$ contribution at x_{ref}, the inner peak, located at $y^+ \approx 16$, has a higher value than the outer peak in the region $y^+ \approx 100$. According to Fig. 24(a), the inner peak is very insensitive to the weak interaction,

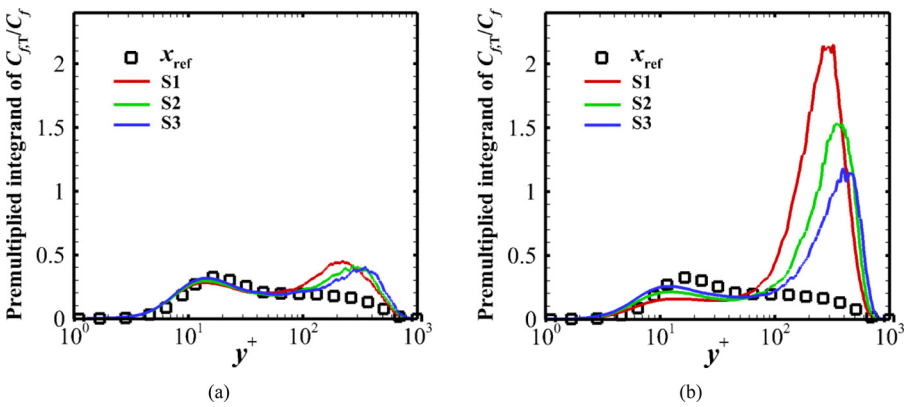

FIG. 24. Pre-multiplied integrands of $C_{f,T}/C_f$ as a function of y^+ at different streamwise locations: (a) shock29 and (b) shock33.2.

while the outer peak experiences a considerable increase, becoming comparable in magnitude at $y^+ \approx 200$–400, implying the increasing importance of the contributions in the outer region. For increasing interaction strength, Fig. 24(b) highlights that the dominance of the inner peak is overtaken by the outer peak. As we can see, the inner peak slightly decreases, with the location being moved closer to the wall, whereas the outer peak dramatically increases, suggesting that most of the $C_{f,\mathrm{T}}$ contribution comes from the outer region at $y^+ > 100$. Recalling the large outer peaks in the wall-normal distributions of pre-multiplied turbulent kinetic energy production discussed in Figs. 16(a) and 16(b), since the $C_{f,\mathrm{T}}$ contribution is associated with the power spent for the TKE production, the reason for the significant amplification of the $C_{f,\mathrm{T}}$ contribution in the outer region induced by the strong interaction becomes apparent.

To investigate what kind of turbulent structures are responsible for the observed amplification of $C_{f,\mathrm{T}}$, we perform a scale decomposition of $C_{f,\mathrm{T}}$ in the spanwise direction, similar to the decomposition method of Duan *et al.*[54] Here, the contribution $C_{f,\mathrm{T}}/C_f$ is expressed as

$$\frac{C_{f,\mathrm{T}}}{C_f} = \int_{-\infty}^{\infty}\int_{-\infty}^{\infty} \frac{k_z y}{C_f}\Phi_{F_T}\,\mathrm{d}(\ln k_z)\mathrm{d}(\ln y), \tag{13}$$

where

$$\Phi_{F_T} = -\bar{\rho}\frac{\partial \widetilde{u}}{\partial y}\Phi_{uv}(k_z,y) = -\bar{\rho}\frac{\partial \widetilde{u}}{\partial y}c_{uv}\left\langle Re\left[\hat{u}(k_z,y)\hat{v}^*(k_z,y)\right]\right\rangle. \tag{14}$$

Here, $\hat{u}$ and $\hat{v}$ denote the Fourier transforms of the streamwise and wall-normal velocity fluctuations, respectively. The superscript asterisk $(*)$, $Re[\bullet]$, and left- and right-angle brackets, respectively, represent the complex conjugate, real part of a complex number, and ensemble averaging. The constant c_{uv} is determined by satisfying

$$\widetilde{u}\widetilde{v} = \int_0^{\infty}\Phi_{uv}(k_z,y)\mathrm{d}k_z. \tag{15}$$

In Fig. 25, contours of the integrand in Eq. (13) at different streamwise locations are shown as functions of normalized wall-normal location y^+ and spanwise wavelength $\lambda_z{}^+$, where a representation of the

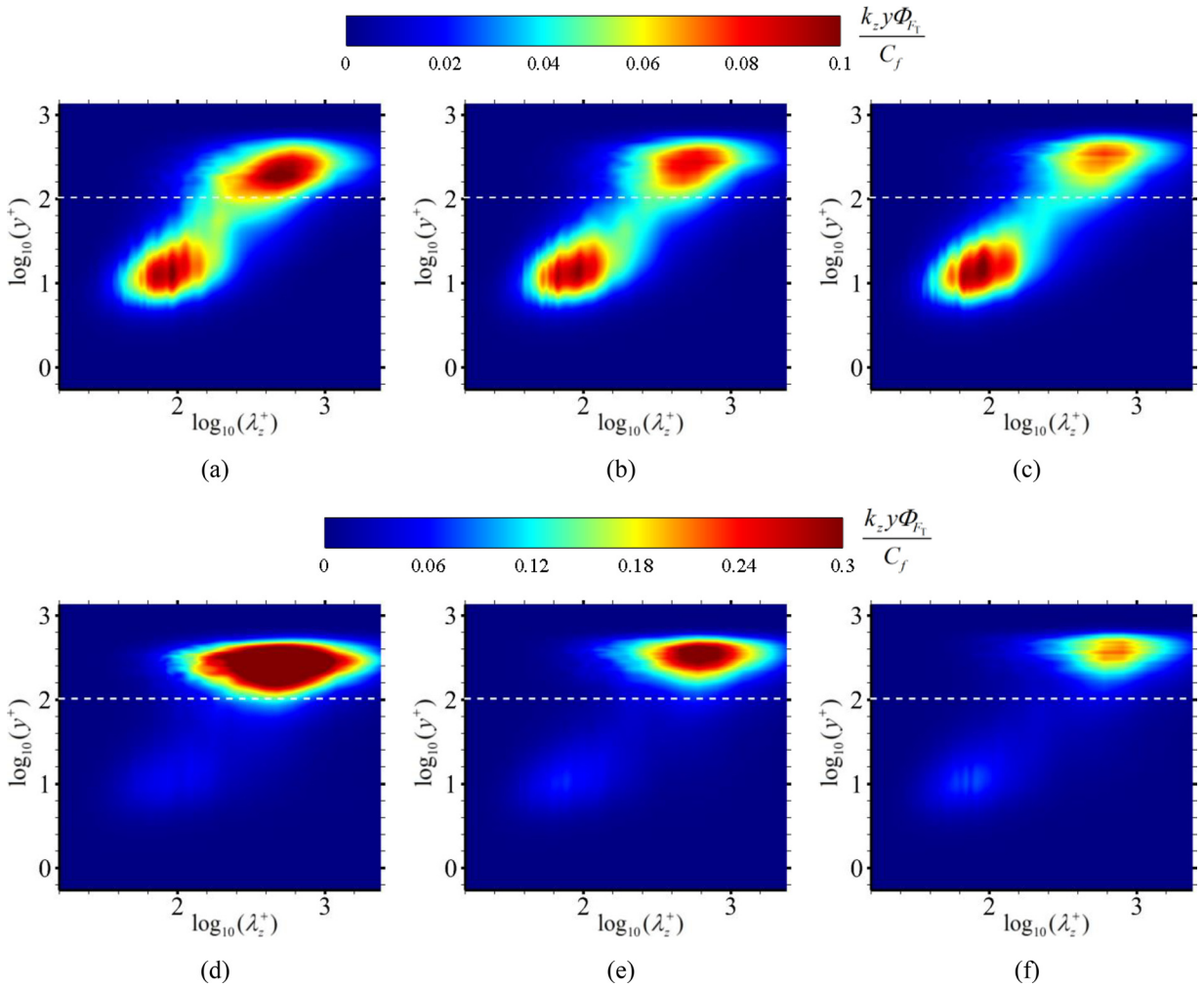

FIG. 25. Contours of $yk_z\Phi_{F_T}/C_f$ at different streamwise locations for the shock29 (upper panels) and shock33.2 (lower panels) cases: (a) and (d) S1; (b) and (e) S2; (c) and (f) S3. The horizontal dashed lines denote $y^+ = 100$.

local contribution to C_f at a given spanwise length scale and a given wall-normal location is displayed. Clearly, the breakdown of the contribution $C_{f,\mathrm{T}}/C_f$ is different in the two flow cases considered. As shown in Figs. 25(a)–25(c), two comparable energy peaks are identified in the weak interaction. To be specific, an inner peak appears at $y^+ \approx 10$, and this is characterized by a spanwise length of $\lambda_z{}^+ \approx 100$, corresponding to the high- and low-speed streaks previously observed in Fig. 8(a). Another energetic peak is located at $y^+ \approx 200$–300 and $\lambda_z{}^+ \approx 500$, and this is ascribed to the readily known large-scale structures in the outer region, as previously discussed in Fig. 9(a).

From examining the values of the two dominant peaks, we believe that the inner small-scale structures make the highest contributions to the C_f generation in the shock29 case. In Figs. 25(d)–25(f), we emphasize that an obvious energization of the outer peak and a sharp decrease in the inner peak are shown in the strong shock interaction. Consequently, the inner peak becomes negligible, experiencing a slight increase from S1 to S3; this can be explained by the slow recovery of the destroyed streaky structures in the inner region, as shown in Fig. 8(b). Importantly, the outer peak dramatically increases, pointing to the increasingly pronounced contributions of the outer large-scale turbulent structures to the mean skin friction generation in the shock33.2 case.

To fully characterize the effect of the interaction strength on the contributions of different length scales to C_f, we have integrated the local contribution of a specific spanwise wavelength $\lambda_z{}^+$ over the entire boundary layer in the two flow cases, where $k_z\Phi_{C_{f,\mathrm{T}}}/C_f$ [with $\Phi_{C_{f,\mathrm{T}}} = \int_0^\infty \Phi_{F_T}(k_z,y)\mathrm{d}y$] is plotted as a function of $\lambda_z{}^+$ in logarithmic scale, as shown in Figs. 26(a) and 26(b), respectively, in such a way that the total area below the curve yields the contribution $C_{f,\mathrm{T}}/C_f$.

Figure 26(a) indicates that in the weak interaction, the mean skin friction is mainly generated in the small-scale region, where the local contribution has a maximum value at $\lambda_z{}^+ \approx 100$. This is associated with the near-wall streaky structures, and it has a secondary small peak in the large-scale region $\lambda_z > 0.5\delta$. In the strong interaction [Fig. 26(b)], all the curves exhibit a pattern different from that observed in the weak interaction, and they are characterized by a single peak in the large range. It can be seen that the three curves are generally moved to the right side of the figure, and the maximum value of the local contribution is attained at $\lambda_z{}^+ \approx 400$–$500$. Following Bernardini and Pirozzoli[55] and Wu *et al.*,[47] we chose a widely used separation wavelength value $\lambda_z{}^+ = 378$ or $\lambda_z = 0.5\delta$ (marked by vertical dashed lines in Fig. 26) to isolate the large-scale contribution. It is found that the contribution coming from the small-scale range is about 65% in the weak interaction, while the large-scale range contributes nearly 58% in the strong interaction. This convincingly demonstrates that the outer large-scale turbulent structures become the dominant contributor in the C_f generation as the interaction strength is increased. Note that despite the integrated contribution being a mixed value associated with the structures in both the inner and outer regions, the role of the inner large-scale structures can be neglected due to the very small values in the lower right corners of the plots in Fig. 25.

E. Mean WHF decomposition

In Sec. III D, the mean skin friction decomposition and the contributions of turbulence structures with different spanwise wavelengths to C_f for the weak and strong interactions were comparatively investigated. The focus of the study in the present section is to establish how the mean WHF generation and the contributions of various turbulent scales may be modified by the effect of interaction strength. For this purpose, we consider the decomposition of mean WHF proposed by Sun *et al.*[13] for C_h at S1–S3 for the two flow cases. This reads as

$$C_h = C_{h,\mathrm{C}} + C_{h,\mathrm{TH}} + C_{h,\mathrm{MD}} + C_{h,\mathrm{TKE}} + C_{h,\mathrm{MS}} + C_{h,\mathrm{RS}} + C_{h,\mathrm{G}}, \tag{16}$$

where

$$C_{h,\mathrm{C}} = \frac{1}{\rho_\infty u_\infty^4}\int_0^\infty k\frac{\partial \bar{T}}{\partial y}\frac{\partial \widetilde{u}}{\partial y}\mathrm{d}y, \tag{17}$$

$$C_{h,\mathrm{TH}} = \frac{1}{\rho_\infty u_\infty^4}\int_0^\infty -c_p\bar{\rho}\widetilde{v''T''}\frac{\partial \widetilde{u}}{\partial y}\mathrm{d}y, \tag{18}$$

$$C_{h,\mathrm{MD}} = \frac{1}{\rho_\infty u_\infty^4}\int_0^\infty (\overline{u''\sigma_{xy}} + \overline{v''\sigma_{yy}})\frac{\partial \widetilde{u}}{\partial y}\mathrm{d}y, \tag{19}$$

$$C_{h,\mathrm{TKE}} = \frac{1}{\rho_\infty u_\infty^4}\int_0^\infty -\frac{1}{2}(\overline{\rho u''u''v''} + \overline{\rho v''v''v''})\frac{\partial \widetilde{u}}{\partial y}\mathrm{d}y, \tag{20}$$

$$C_{h,\mathrm{MS}} = \frac{1}{\rho_\infty u_\infty^4}\int_0^\infty (\widetilde{u}\bar{\sigma}_{xy} + \widetilde{v}\bar{\sigma}_{yy})\frac{\partial \widetilde{u}}{\partial y}\mathrm{d}y, \tag{21}$$

$$C_{h,\mathrm{RS}} = \frac{1}{\rho_\infty u_\infty^4}\int_0^\infty -\bar{\rho}(\widetilde{u}\widetilde{u''v''} + \widetilde{v}\widetilde{v''v''})\frac{\partial \widetilde{u}}{\partial y}\mathrm{d}y, \tag{22}$$

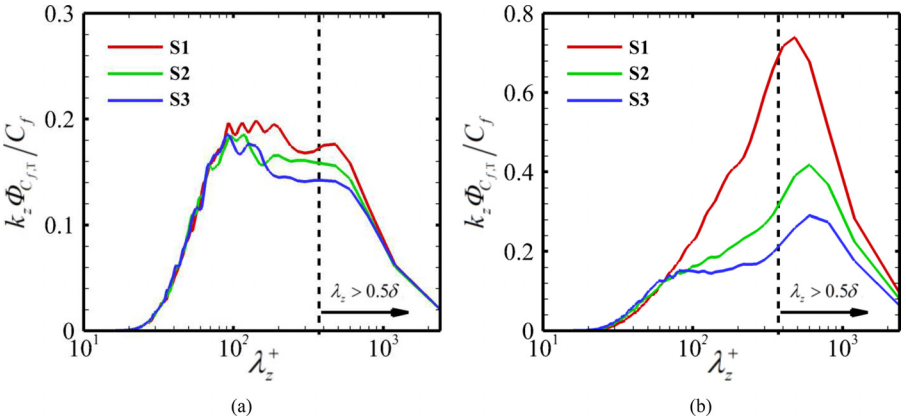

FIG. 26. Distribution of local contribution $k_z\Phi_{C_{f,\mathrm{T}}}/C_f$ as a function of spanwise length scale $\lambda_z{}^+$ for the (a) shock29 and (b) shock33.2 cases.

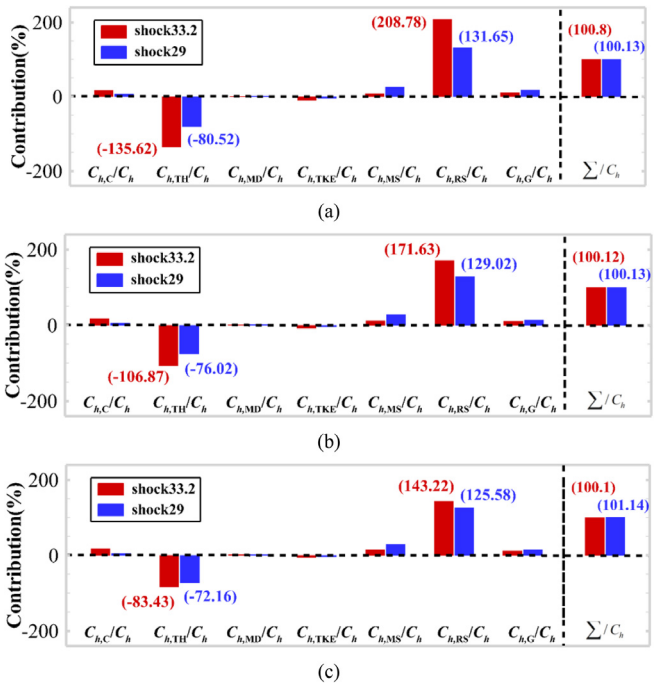

FIG. 27. Contributions to C_h at different streamwise locations: (a) S1; (b) S2; (c) S3.

$$C_{h,\mathrm{G}} = \frac{1}{\rho_\infty u_\infty^4}\int_0^\infty (\tilde{u}-u_\infty)\left[\rho\frac{D\tilde{E}}{Dt}+\frac{\partial(\tilde{u}\bar{p})}{\partial x}+\frac{\partial(\tilde{v}\bar{p})}{\partial y}\right.$$
$$-\left(k\frac{\partial\bar{T}}{\partial x}-c_p\bar{\rho}\widetilde{u''T''}+\overline{u''\sigma_{xx}}+\overline{v''\sigma_{yx}}-\frac{1}{2}\overline{\rho u''u''u''}\right.$$
$$\left.\left.-\frac{1}{2}\overline{\rho v''v''u''}+\tilde{u}\bar{\sigma}_{xy}+\tilde{v}\bar{\sigma}_{yy}-\tilde{u}\overline{\rho u''u''}-\tilde{v}\overline{\rho v''u''}\right)\right]\mathrm{d}y. \tag{23}$$

Here, the six terms $C_{h,\mathrm{C}}$, $C_{h,\mathrm{TH}}$, $C_{h,\mathrm{MD}}$, $C_{h,\mathrm{TKE}}$, $C_{h,\mathrm{MS}}$, and $C_{h,\mathrm{RS}}$ account for the mean heat conduction, turbulent transport of heat, wall-normal component of molecular diffusion, turbulent transport of TKE, and work of the molecular stresses and Reynolds stresses, respectively. The term $C_{h,\mathrm{G}}$ is expected to be responsible for spatial growth of the flow, including the variation of the specific total energy with time, the work of pressure, and the streamwise heterogeneity.

The full compositions of C_h at different streamwise locations are compared in Figs. 27(a)–27(c), respectively. For all locations, the sum of the seven decomposed components agrees very well with the directly calculated values based on the original definition; the relative errors, calculated by $\sum/C_h - 1$, are confined within $\pm 0.2\%$, which verifies the accuracy of the present decomposition. It appears that the generation mechanism of C_h in the downstream region is the same with both the weak and strong shock interactions, which is quite different from what we have found in the generation of C_f. For the upstream TBL, the balance between a large positive $C_{h,\mathrm{RS}}$ and a large negative $C_{h,\mathrm{TH}}$ mainly dominates the mean WHF generation at x_{ref}; these values are about 126.67% and –76.64% of C_h, respectively. This trend can be explained as the result of the excessive heat at the wall generated by the work of the Reynolds stresses being carried away from the wall toward the outer region through the turbulent transport of heat. According to the decompositions given in Figs. 27(a)–27(c), we highlight that although both $C_{h,\mathrm{RS}}$ and $C_{h,\mathrm{TH}}$ experience a consistent decrease in magnitude as the probe moves downstream, a similar conclusion is made at S1–S3 for the two flow cases; namely, the overshoot of the large positive $C_{h,\mathrm{RS}}$ is mostly balanced by the large negative $C_{h,\mathrm{TH}}$. However, it is worth noting that the greatest difference between the weak and strong interaction lines in the local contribution lies at a particular wall-normal location, which is clearly displayed by the pre-multiplied integrands of $C_{h,\mathrm{RS}}/C_h$ and $C_{h,\mathrm{TH}}/C_h$, as reported in Figs. 28(a) and 28(b), respectively.

Figure 28(a) shows that the curve shapes of the pre-multiplied integrands in the weak interaction are similar to that at x_{ref}, but the local contribution in the inner region $y^+ < 100$ is relatively decreased for both $C_{h,\mathrm{RS}}$ and $C_{h,\mathrm{TH}}$, and considerable increases occur in the outer layer when compared to those at x_{ref}. For the strong interaction, the results in Fig. 28(b) reveal that increasing the shock angle from 29° to 33.2° does change the curve shape and peak location. A dominant peak, located at $y^+ = 400$–600, is clearly presented, suggesting that most of $C_{h,\mathrm{RS}}/C_h$ and $C_{h,\mathrm{TH}}/C_h$ are associated with the turbulent structures in the outer layer. This energization of the outer layer is very similar to that observed in the pre-multiplied integrand of $C_{f,\mathrm{T}}/C_f$, as

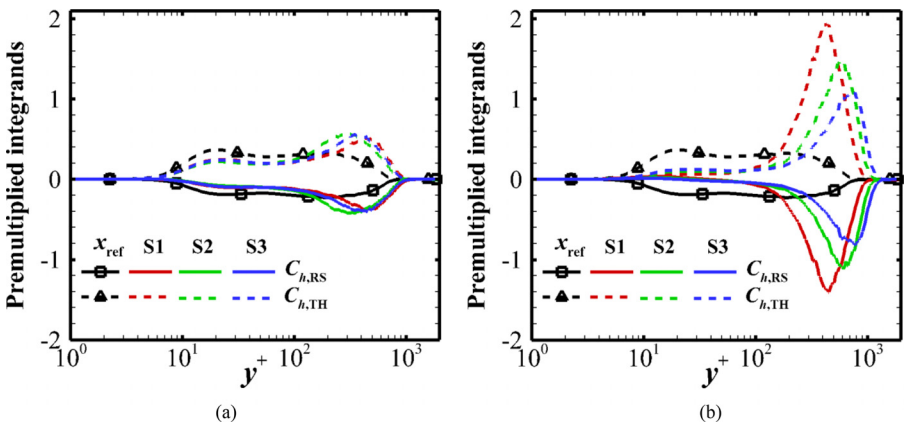

FIG. 28. Pre-multiplied integrands of $C_{h,\mathrm{RS}}/C_h$ and $C_{h,\mathrm{TH}}/C_h$ as functions of y^+ at different streamwise locations: (a) shock29; (b) shock33.2.

examined in Fig. 24. This supports a leading role for the outer structures in the generation of C_h.

Analogous to the contribution $C_{f,\mathrm{T}}/C_f$ rewritten in Eq. (13), we can also rewrite the contributions of $C_{h,\mathrm{RS}}/C_h$ and $C_{h,\mathrm{TH}}/C_h$ as

$$\frac{C_{h,\mathrm{RS}}}{C_h} = \int_{-\infty}^{\infty}\int_{-\infty}^{\infty} \frac{k_z y}{C_h}\Phi_{\mathrm{RS}}\mathrm{d}(\ln k_z)\mathrm{d}(\ln y), \tag{24}$$

$$\frac{C_{h,\mathrm{TH}}}{C_h} = \int_{-\infty}^{\infty}\int_{-\infty}^{\infty} \frac{k_z y}{C_h}\Phi_{\mathrm{TH}}\mathrm{d}(\ln k_z)\mathrm{d}(\ln y), \tag{25}$$

where

$$\Phi_{\mathrm{RS}} = -\bar{\rho}\widetilde{u}\frac{\partial \widetilde{u}}{\partial y}\Phi_{uv}(k_z,y) = -\bar{\rho}\widetilde{u}\frac{\partial \widetilde{u}}{\partial y}c_{uv}\left\langle Re\left[\hat{u}(k_z,y)\hat{v}^*(k_z,y)\right]\right\rangle, \tag{26}$$

$$\Phi_{\mathrm{TH}} = -c_p\bar{\rho}\frac{\partial \widetilde{u}}{\partial y}\Phi_{vT}(k_z,y) = -c_p\bar{\rho}\frac{\partial \widetilde{u}}{\partial y}c_{vt}\left\langle Re\left[\hat{v}(k_z,y)\hat{T}^*(k_z,y)\right]\right\rangle. \tag{27}$$

Note that the contribution associated with the wall-normal component of the Reynolds stress is less than 5% of $C_{h,\mathrm{RS}}$, which is neglected in Eq. (26), and the constant c_{vt} in Eq. (27) is determined using a similar approach as that of c_{uv} given in Eq. (15). The variable c_p denotes the specific heat capacity of gas at a constant pressure.

To further discuss the effect of the interaction strength on the breakdown of $C_{h,\mathrm{RS}}/C_h$ and $C_{h,\mathrm{TH}}/C_h$, we concentrate on the integrands in Eqs. (24) and (25), which are plotted as functions of y^+ and $\lambda_z{}^+$ with logarithmic scales in Figs. 29 and 30, respectively. Regarding the $C_{h,\mathrm{RS}}/C_h$ contribution, the energetic outer peaks in Figs. 29(d)–29(f), compared with those in Figs. 29(a)–29(c), are consistent with the findings for $C_{f,\mathrm{T}}/C_f$ as considered previously in Fig. 25. Likewise, the local contributions associated with the outer large-scale structures at ($y^+ > 100$, $\lambda_z{}^+ > 400$) are dramatically increased when the interaction becomes stronger, whereas the inverse behavior is apparently observed in the inner region featured by the small-scale structures; this is clearly reflected by the negligibly small peaks at $y^+ \approx 15$ and $\lambda_z{}^+ \approx 100$ in Figs. 29(a)–29

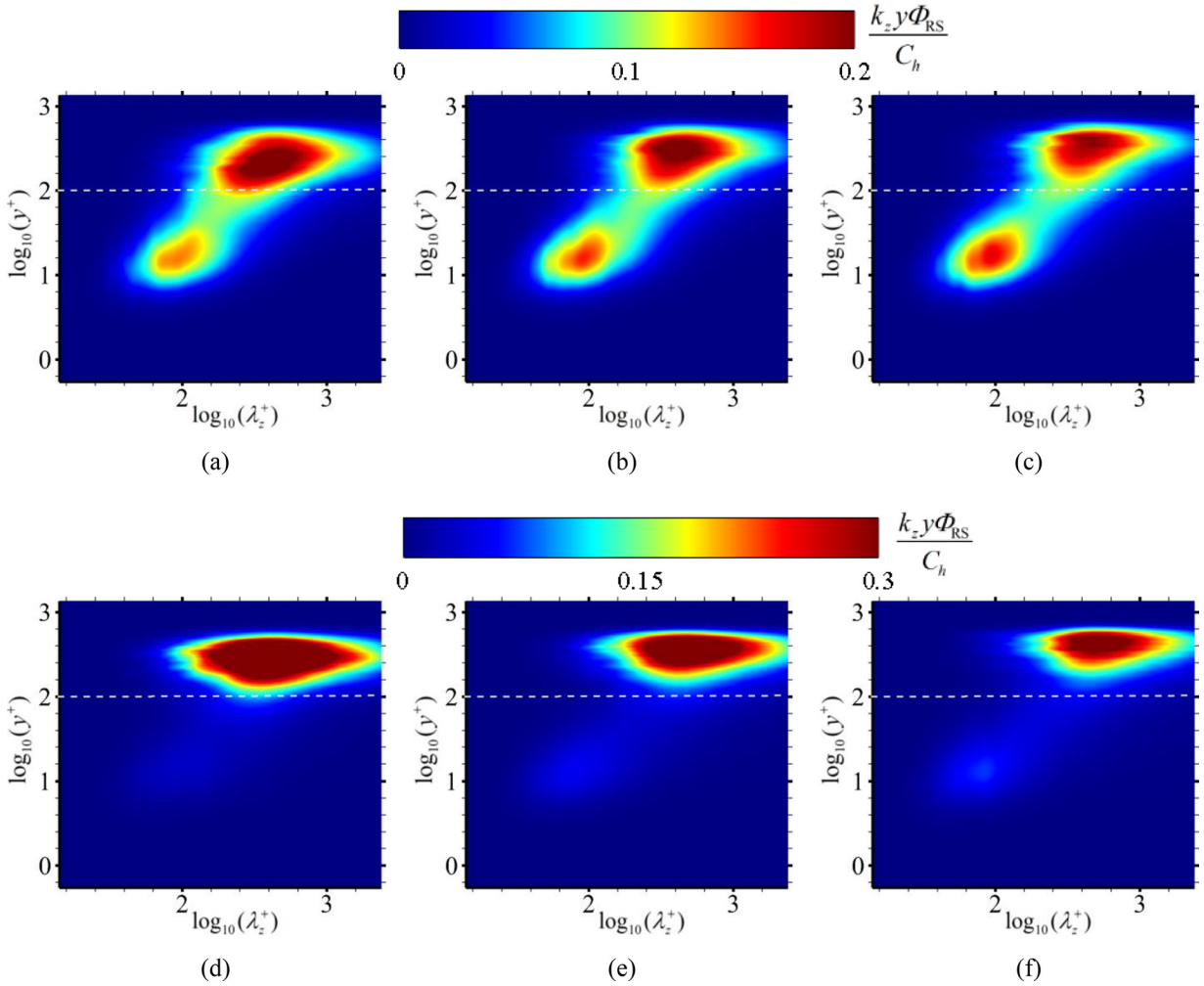

FIG. 29. Contours of $yk_z\Phi_{\mathrm{RS}}/C_h$ at different streamwise locations for the shock29 (upper panels) and shock33.2 (lower panels) cases: (a) and (d) S1; (b) and (e) S2; (c) and (f) S3. The horizontal dashed lines denote $y^+ = 100$.

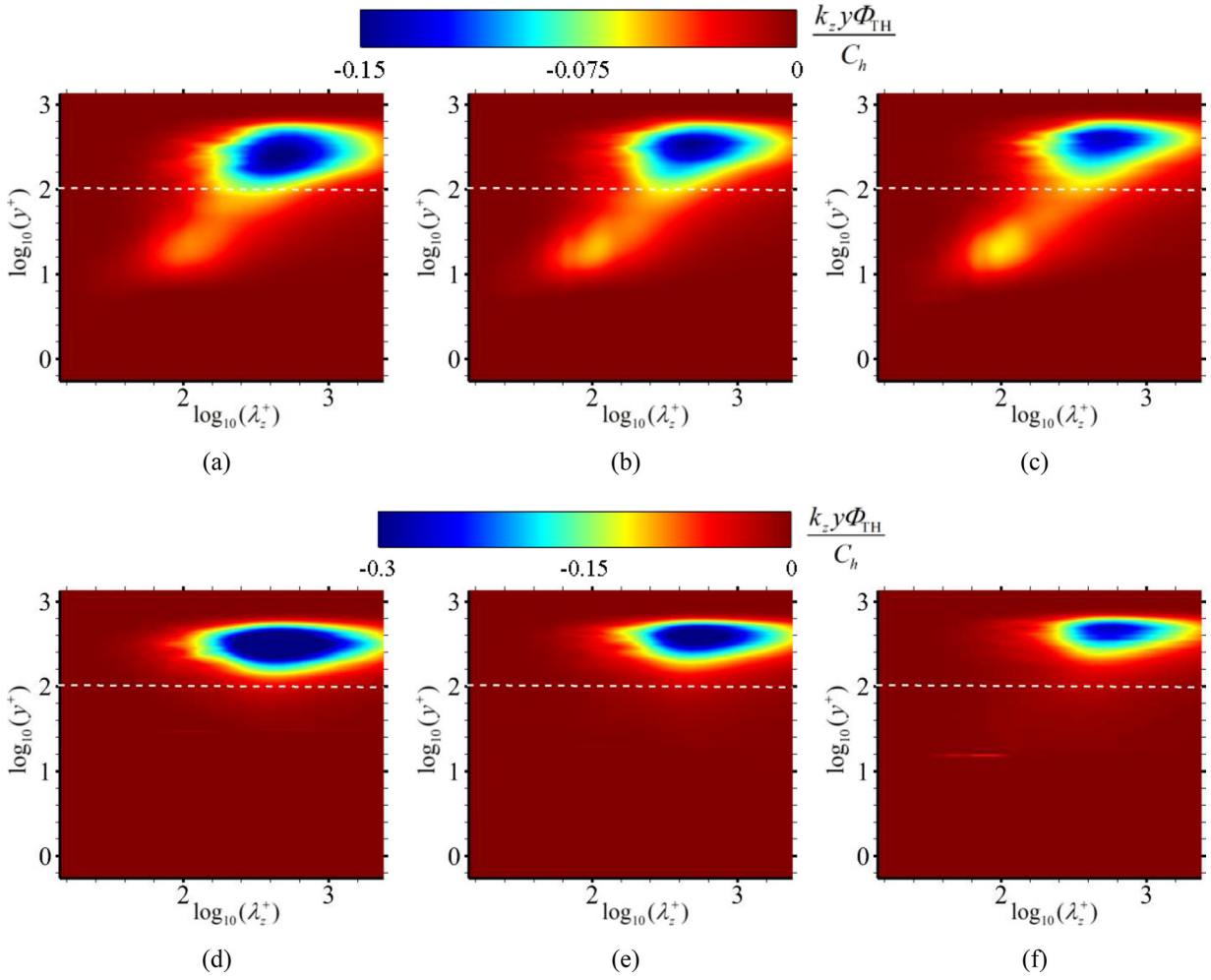

FIG. 30. Contours of $yk_z\Phi_{TH}/C_h$ at different streamwise locations for the shock29 (upper panels) and shock33.2 (lower panels) cases: (a) and (d) S1; (b) and (e) S2; (c) and (f) S3. The horizontal dashed lines denote $y^+ = 100$.

(c). These close similarities between the two contributions $C_{h,RS}/C_h$ and $C_{f,T}/C_f$ are not surprising: the integrands in Eqs. (13) and (24) are nearly the same, aside from an additional mean quantity $\widetilde{u}$ in the spectra Φ_{RS} [see Eq. (26)].

In Figs. 30(d)–30(f), an obvious energization of the outer large-scale structures, caused by the increased interaction strength, is evidently observed in the breakdown of $C_{h,TH}/C_h$, implying that the turbulent transport of heat in the downstream relaxation region is mainly characterized by the outer large-scale structures in the shock33.2 case. However, we remark that even in the case of the weak interaction, a large proportion of $C_{h,TH}/C_h$ is related to the outer large-scale structures; this can be seen from the dominant outer peaks occurring at $y^+ > 100$ and the negligible inner peaks in Figs. 30(a)–30(c). This finding is quite different from the observations of the $C_{h,RS}/C_h$ contribution in Figs. 29(a)–29(c), where the inner and outer peaks are relatively comparable in magnitude for the shock29 case. It is reasonably inferred that the streaky structures in the inner region are not the determinant of the $C_{h,TH}$ contribution in either the weak or the strong interaction.

Similar to Fig. 26, in Figs. 31(a) and 31(b), the local contributions of specific spanwise wavelengths λ_z^+ to $C_{h,RS}/C_h$ and $C_{h,TH}/C_h$ are directly compared by plotting $k_z\Phi_{C_{h,RS}}/C_h$ and $k_z\Phi_{C_{h,TH}}/C_h$, respectively, as functions of λ_z^+ in logarithmic scale, where $\Phi_{C_{h,RS}} = \int_0^\infty \Phi_{RS}(k_z,y)dy$ and $\Phi_{C_{h,TH}} = \int_0^\infty \Phi_{TH}(k_z,y)dy$. It is expected that the large-scale structures at $\lambda_z^+ > 378$ or $\lambda_z > 0.5\delta$ will make the dominant contributions to C_h when the interaction strength is increased. For $C_{h,RS}/C_h$, the small-scale components at $\lambda_z^+ < 378$ or $\lambda_z < 0.5\delta$ are dominant in the shock29 case, accounting for about 60% of $C_{h,RS}/C_h$; an opposite behavior is found in the shock33.2 case, with the large-scale components contributing 55%–60% of $C_{h,RS}/C_h$ at S1–S3. For $C_{h,TH}/C_h$, the contributions of the large-scale components in the two cases are about 53% and 71%, respectively, which demonstrates the qualitative observations in Fig. 30. Putting these results together with those made regarding the contribution of $C_{f,T}/C_f$ in Fig. 26 and the production of TKE in Fig. 16, we can conclude that the large-scale structures in the outer layer are energetically relevant in the recovery process downstream of the strong interaction.

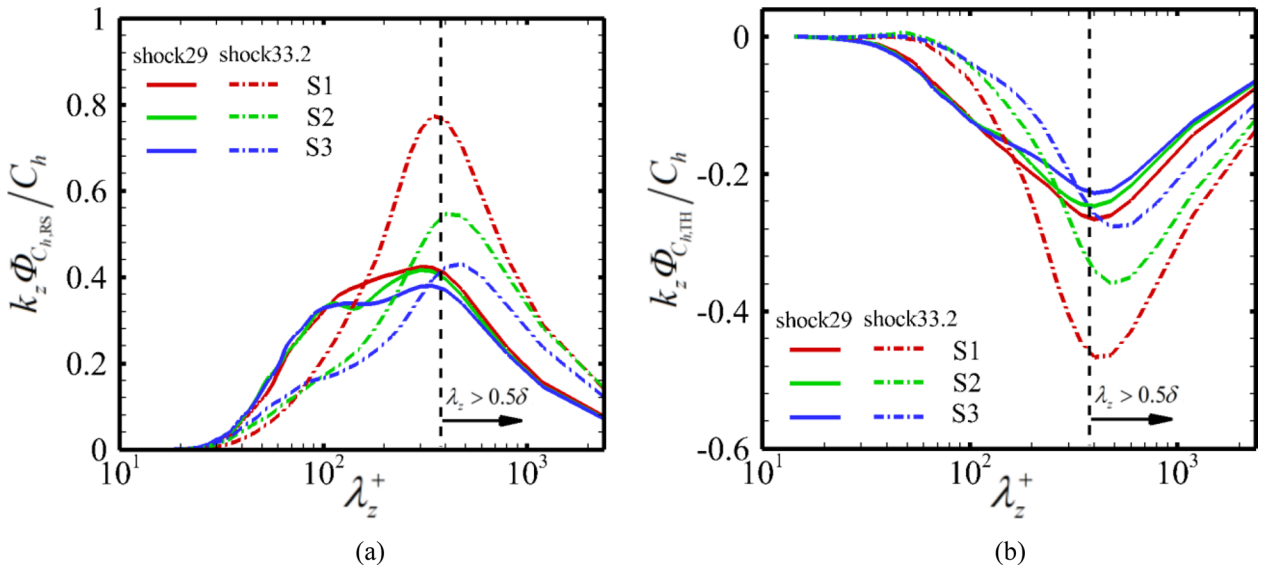

FIG. 31. Distribution of local contribution (a) $k_z\Phi_{C_{h,RS}}/C_h$ and (b) $k_z\Phi_{C_{h,TH}}/C_h$ as a function of spanwise length scale λ_z^+.

One possible explanation for the energization of the outer-layer large-scale structures is the formation of Görtler-type vortices in the downstream relaxation region, which has often been quoted in previous studies of SWTBLI flows. Indeed, Pasquariello *et al.*[56] and Zhuang *et al.*[57] reported that the Görtler-type vortices are characterized by a spanwise length scale of the order of the upstream turbulent boundary layer thickness δ. In the present study, the dominant spanwise lengths at S3 in Figs. 26(b) and 31 are about 0.8δ, very close to the characteristic value. Evidence can further be found from the Görtler number, as given by Simits and Dussauge.[58] It is found that the values of the calculated Görtler number in the strong interaction are much higher than the critical value of 0.6, which is noted by Loginov *et al.*,[59] implying that the Görtler-type vortices are more likely to be formed in the shock33.2 case.

IV. CONCLUSIONS

In the present study, we perform DNS of the interaction of an impinging shock wave with a spatially developing supersonic turbulent boundary layer on a flat plate at Mach number $M_\infty = 2.25$ and friction Reynolds number $Re_\tau = 769$ to investigate the influence of the interaction strength on the recovery process in the downstream region. Two incident shock angles (29° and 33.2°) corresponding to the weak and strong interactions are considered; the mean flow in the weak interaction is attached, and a separation bubble is observed in the strong interaction.

The effect of the interaction strength on the evolution of turbulence in the recovery process is comparatively analyzed. It is found that the Reynolds stress components experience a rather quick recovery in the weak interaction, exhibiting close similarities to those of the upstream TBL. As the interaction strength increases, a significant amplification of the Reynolds stresses is particularly observed in the outer region of the reattached boundary layer. The anisotropy of the Reynolds stresses is relatively preserved in the weak interaction, whereas the near-wall turbulent state is significantly changed by the increased interaction strength, showing a slow reversal tendency in the anisotropy-invariant map. Moreover, the TKE budgets exhibit the behavior typically observed in zero-pressure-gradient TBLs, except for the increasingly pronounced importance of the outer-layer large-scale structures for the TKE production in the strong interaction.

We show that increasing the interaction strength has a significant influence on the statistical and structural properties of wall pressure fluctuations in the downstream region. It is observed that the recovery of the dynamic pressure in both flow cases is uncompleted. The fluctuations, when made non-dimensional using the local rms value, yield good collapse of the PDF curves, and the pre-multiplied spectra of the fluctuating wall pressure suggest that the characteristic frequencies decrease as the interaction strength is increased. In addition, the spatial and temporal properties of the wall pressure fluctuations are investigated by space–time correlation analysis. It is found that an increased interaction strength leads to an increase in the spatial extent and a decrease in the convection velocity.

The effect of the interaction strength has a clear impact on the generation mechanism of the mean skin friction. We highlight that a large positive contribution from $C_{f,\mathrm{T}}$, associated with TKE production, and a positive large contribution from $C_{f,\mathrm{V}}$, related to the direct effect of viscous dissipation, are dominant in the weak interaction, similar to the values found in the upstream TBL; conversely, the contribution from $C_{f,\mathrm{G}}$ responsible for the spatial growth of the flow becomes negative and large in the strong interaction, counteracting the overshoot of the large positive $C_{f,\mathrm{T}}$. Regarding the mean wall heat flux, the decomposition analysis shows two dominant contributions in the recovery process: a large positive contribution from $C_{h,\mathrm{RS}}$ caused by the work of the Reynolds stresses, and a large negative contribution from $C_{h,\mathrm{TH}}$ accounting for turbulent transport of heat. We find that the balance between $C_{h,\mathrm{RS}}$ and $C_{h,\mathrm{TH}}$ is very insensitive to the interaction strength. Using a scale-decomposition method, we quantitatively compare the scale-dependent differences between the two reflected interactions. We reveal that an increased interaction

strength dramatically decreases the contribution of the small-scale structures in the inner layer and apparently enhances the significance of the outer-layer large-scale structures in contributing to C_f and C_h.

ACKNOWLEDGMENTS

This study was supported by the National Key R&D Program of China (Grant No. 2019YFA0405300) and the National Natural Science Foundation of China (Grant Nos. 11972356 and 91852203).

AUTHOR DECLARATIONS

Conflict of Interest

The authors have no conflicts to disclose.

Author Contributions

Fulin Tong: Conceptualization (equal); Writing – original draft (equal). **Jiang Lai:** Validation (lead). **Junyi Duan:** Writing – review & editing (equal). **Siwei Dong:** Writing – review & editing (equal). **Xianxu Yuan:** Conceptualization (equal). **Xinliang Li:** Software (lead).

DATA AVAILABILITY

The data that support the findings of this study are available from the corresponding author upon reasonable request.

REFERENCES

[1]D. S. Dolling, "Fifty years of shock-wave/boundary layer interaction research: What next?," AIAA J. **39**(8), 1517–1531 (2001).
[2]D. V. Gaitonde, "Progress in shock wave/boundary layer interactions," Prog. Aerosp. Sci. **72**, 80–99 (2015).
[3]N. T. Clemens and V. Narayanaswamy, "Low-frequency unsteadiness of shock wave/turbulent boundary layer interactions," Annu. Rev. Fluid Mech. **46**, 469–492 (2014).
[4]D. S. Dolling and C. T. Or, "Unsteadiness of the shock wave structure in attached and separated compression ramp flow fields," AIAA Paper No. 1983-1715, 1983.
[5]P. Dupont, C. Haddad, and J. F. Debieve, "Space and time organization in a shock-induced separated boundary layer," J. Fluid Mech. **559**, 255–277 (2006).
[6]B. Morgan, K. Duraisamy, N. Nguyen, S. Kawai, and S. K. Lele, "Flow physics and RANS modeling of oblique shock/turbulent boundary layer interaction," J. Fluid Mech. **729**, 231–284 (2013).
[7]L. J. Souverein, P. Dupont, J. F. Debiève, and J. P. Dussauge, "Effect of interaction strength on unsteadiness in turbulent shock-wave-induced separations," AIAA J. **48**(7), 1480–1493 (2010).
[8]A. Jammalamadaka, Z. R. Li, and F. Jaberi, "Numerical investigations of shock wave interactions with a supersonic turbulent boundary layer," Phys. Fluids **26**, 056101 (2014).
[9]A. M. Schreyer, D. Sahoo, O. J. H. Williams, and A. J. Smits, "Experimental investigation of two hypersonic shock/turbulent boundary-layer interactions," AIAA J. **56**(12), 4830–4844 (2018).
[10]M. A. Mustafa, N. J. Parziale, M. S. Smith, and E. C. Marineau, "Amplification and structure of streamwise-velocity fluctuations in compression-corner shock-wave/turbulent boundary-layer interactions," J. Fluid Mech. **863**, 1091–1122 (2019).
[11]H. Babinsky and J. K. Harvey, *Shock Wave–Boundary-Layer Interactions* (Cambridge University Press, 2011).
[12]W. P. Li, Y. T. Fan, D. Modesti, and C. Cheng, "Decomposition of the mean skin-friction drag in compressible turbulent channel flows," J. Fluid Mech. **875**, 101–123 (2019).
[13]D. Sun, Q. L. Guo, X. X. Yuan, H. Y. Zhang, and C. Li, "A decomposition formula for the wall heat flux of a compressible boundary layer," Adv. Aerodyn. **3**, 33 (2021).
[14]F. L. Tong, S. W. Dong, J. Lai, X. X. Yuan, and X. L. Li, "Wall shear stress and wall heat flux in a supersonic turbulent boundary layer," Phys. Fluids **34**, 015127 (2022).
[15]F. L. Tong, X. X. Yuan, J. Lai, J. Y. Duan, D. Sun, and S. W. Dong, "Wall heat flux in a supersonic shock wave/turbulent boundary layer interaction," Phys. Fluids **34**, 065104 (2022).
[16]F. L. Tong, X. L. Li, Y. H. Duan, and C. P. Yu, "Direct numerical simulation of supersonic turbulent boundary layer subjected to a curved compression ramp," Phys. Fluids **29**, 125101 (2017).
[17]F. L. Tong, C. P. Yu, Z. G. Tang, and X. L. Li, "Numerical studies of shock wave interactions with a supersonic turbulent boundary layer in compression corner: Turning angle effects," Comput. Fluids **149**, 56–69 (2017).
[18]F. L. Tong, J. Y. Duan, and X. L. Li, "Characteristics of reattached boundary layer in shock wave and turbulent boundary layer interaction," Chin. J. Aeronaut. **35**(6), 172–185 (2022).
[19]F. L. Tong, D. Sun, and X. L. Li, "Direct numerical simulation of impinging shock wave and turbulent boundary layer interaction over a wavy-wall," Chin. J. Aeronaut. **34**(5), 350–363 (2021).
[20]X. L. Li, D. X. Fu, and Y. W. Ma, "Direct numerical simulation of hypersonic boundary-layer transition over a blunt cone," AIAA J. **46**(11), 2899–2913 (2008).
[21]X. L. Li, D. X. Fu, and Y. W. Ma, "Direct numerical simulation of hypersonic boundary layer transition over a blunt cone with a small angle of attack," Phys. Fluids **22**, 025105 (2010).
[22]M. P. Martin, E. M. Taylor, M. Wu, and V. G. Weirs, "A bandwidth-optimized WENO scheme for the effective direction numerical simulation of compressible turbulence," J. Comput. Phys. **220**, 270–289 (2006).
[23]M. Wu and M. P. Martin, "Direct numerical simulation of supersonic turbulent boundary layer over a compression ramp," AIAA J. **45**(4), 879–889 (2007).
[24]S. Gottlieb and C. W. Shu, "Total variation diminishing Runge–Kutta schemes," Math. Comput. **67**, 73–85 (1998).
[25]S. Pirozzoli and F. Grasso, "Direct numerical simulation of impinging shock wave/turbulent boundary layer interaction at M = 2.25," Phys. Fluids **18**, 065113 (2006).
[26]S. Priebe, M. Wu, and M. P. Martin, "Direct numerical simulation of a reflected-shock-wave/turbulent-boundary-layer interaction," AIAA J. **47**(5), 1173–1185 (2009).
[27]J. Fang, A. A. Zheltovodov, Y. F. Yao, C. Moulinec, and D. R. Emerson, "On the turbulence amplification in shock-wave/turbulent boundary layer interaction," J. Fluid Mech. **897**, A32 (2020).
[28]S. Pirozzoli, F. Grasso, and T. B. Gatski, "Direct numerical simulation and analysis of a spatially evolving supersonic turbulent boundary layer at M = 2.25," Phys. Fluids **16**, 530 (2004).
[29]P. Schlatter and R. Örlü, "Assessment of direct numerical simulation data of turbulent boundary layers," J. Fluid Mech. **659**, 116–126 (2010).
[30]L. Duan, M. M. Choudhari, and C. Zhang, "Pressure fluctuations induced by a hypersonic turbulent boundary layer," J. Fluid Mech. **804**, 578–607 (2016).
[31]X. Wu and P. Moin, "Direct numerical simulation of turbulence in a nominally zero-pressure-gradient flat-plate boundary layer," J. Fluid Mech. **630**, 5–41 (2009).
[32]P. R. Spalart, "Direct numerical simulation of a turbulent boundary layer up to $Re_\theta = 1410$," J. Fluid Mech. **187**, 61–98 (1988).
[33]M. S. Shadloo, A. Hadjadj, and F. Hussain, "Statistical behavior of supersonic turbulent boundary layers with heat transfer at $M_\infty = 2$," Int. J. Heat Fluid Flow **53**, 113–134 (2015).
[34]S. Pirozzoli, M. Bernardini, and F. Grasso, "Direct numerical simulation of transonic shock/boundary layer interaction under conditions of incipient separation," J. Fluid Mech. **657**, 361–393 (2010).
[35]J. C. del Álamo and J. Jiménez, "Spectra of the very large anisotropic scales in turbulent channels," Phys. Fluids **15**, L41–L44 (2003).
[36]S. Pirozzoli, M. Bernardini, and F. Grasso, "Characterization of coherent vertical structures in a supersonic turbulent boundary layer," J. Fluid Mech. **613**, 205–231 (2008).
[37]S. K. Robinson, "Coherent motions in the turbulent boundary layer," Annu. Rev. Fluid Mech. **23**, 601–639 (1991).
[38]S. Pirozzoli and M. Bernardini, "Turbulence in supersonic boundary layers at moderate Reynolds number," J. Fluid Mech. **688**, 120–168 (2011).

[39]M. Grilli, S. Hickel, and N. A. Adams, "Large-eddy simulation of a supersonic turbulent boundary layer over a compression–expansion ramp," Int. J. Heat Fluid Flow **42**, 79–93 (2013).
[40]J. Jeong and F. Hussain, "On the identification of a vortex," J. Fluid Mech. **285**, 69–94 (1995).
[41]M. Hayshi, A. Sakurai, and S. Aso, "Measurement of heat-transfer coefficients in shock wave-turbulent boundary layer interaction regions with a multi-layered thin film heat transfer gauge," NASA Technical Memo No. TM 77958, 1986.
[42]P. S. Volpiani, M. Bernardini, and J. Larsson, "Effects of a nonadiabatic wall on supersonic shock/boundary layer interactions," Phys. Rev. Fluids **3**, 083401 (2018).
[43]J. L. Lumley, "Computational modeling of turbulent flows," Adv. Appl. Mech. **18**, 123–176 (1978).
[44]M. B. Sun, N. D. Sandham, and Z. W. Hu, "Turbulence structures and statistics of a supersonic turbulent boundary layer subjected to concave surface curvature," J. Fluid Mech. **865**, 60–99 (2019).
[45]S. Priebe and M. P. Martin, "Turbulence in a hypersonic compression ramp flow," Phys. Rev. Fluids **6**, 034601 (2021).
[46]S. Pirozzoli and M. Bernardini, "Direct numerical simulation database for impinging shock wave/turbulent boundary-layer interaction," AIAA J. **49**(6), 1307–1312 (2011).
[47]X. S. Wu, J. H. Liang, and Y. X. Zhao, "Direct numerical simulation of a supersonic turbulent boundary layer subjected to a concave surface," Phys. Rev. Fluids **4**, 044602 (2019).
[48]M. Bernardini and S. Pirozzoli, "Wall pressure fluctuations beneath supersonic turbulent boundary layers," Phys. Fluids **23**, 085102 (2011).
[49]M. K. Bull, "Wall pressure fluctuations associated with subsonic turbulent boundary layer flow," J. Fluid Mech. **28**, 719–754 (1967).
[50]M. Bernardini, S. Pirozzoli, and F. Grasso, "The wall pressure signature of transonic shock/boundary layer interaction," J. Fluid Mech. **671**, 288–312 (2011).
[51]W. W. Willmarth, "Wall pressure fluctuations beneath turbulent boundary layers," Annu. Rev. Fluid Mech. **7**, 13–36 (1975).
[52]N. Renard and S. Deck, "A theoretical decomposition of mean skin friction generation into physical phenomena across the boundary layer," J. Fluid Mech. **790**, 339–367 (2016).
[53]Y. T. Fan, W. P. Li, M. Atzori, R. Pozuelo, P. Schlatter, and R. Vinuesa, "Decomposition of the mean skin-friction drag in adverse-pressure-gradient turbulent boundary layers," Phys. Rev. Fluids **5**, 114608 (2020).
[54]Y. C. Duan, Q. Zhong, G. Q. Wang, P. Zhang, and D. X. Li, "Contributions of different scales of turbulent motions to the mean wall-shear stress in open channel flows at low-to-moderate Reynolds numbers," J. Fluid Mech. **918**, A40 (2021).
[55]M. Bernardini and S. Pirozzoli, "Inner/outer layer interactions in turbulent boundary layers: A refined measure for the large-scale amplitude modulation mechanism," Phys. Fluids **23**, 061701 (2011).
[56]V. Pasquariello, S. Hickel, and N. A. Adams, "Unsteady effects of strong shock-wave/boundary-layer interaction at high Reynolds number," J. Fluid Mech. **823**, 617–657 (2017).
[57]Y. Xhuang, H. J. Tan, X. Li, F. J. Sheng, and Y. C. Zhang, "Görtler-like vortices in an impinging shock wave/turbulent boundary layer interaction flow," Phys. Fluids **30**, 061702 (2018).
[58]A. J. Smits and J. P. Dussauge, *Turbulent Shear Layers in Supersonic Flow* (Springer, 2006).
[59]M. S. Loginov, N. A. Adams, and A. A. Zheltovodov, "Large-eddy simulation of shock-wave/turbulent-boundary-layer interaction," J. Fluid Mech. **565**, 135–169 (2006).